Theoretical Studies of Adhesive Interactions between Silica Surface and Polymers

樋口, 千紗

https://hdl.handle.net/2324/4475067

出版情報：Kyushu University, 2020, 博士（工学）, 課程博士
バージョン：
権利関係：

Theoretical Studies of Adhesive Interactions between Silica Surface and Polymers

Chisa Higuchi

Department of Chemistry and Biochemistry

Graduate School of Engineering

Kyushu University

Table of Contents

Chapter 1. General Introduction

1-1. Adhesion technology and epoxy resins

Adhesion technology is widely used in various industries, such as construction, automotive, aerospace, sports equipment, and electronics, due to its lightness, mechanical strength, and insulation properties.[1] Adhesion technology has been advancing day by day, and a lot of experimental-based research has been conducted for various applications.[2,3,4] However, the principles underlying it are not fully understood due to its complexity. In other words, the theory of adhesion is still in its infancy, leaving the possibility for new research.

One of the most common adhesives, epoxy resins can be readily employed in many manufacturing processes, including pultrusion, molding, and coating.[5] Excellent physical properties of epoxy resins include toughness, durability, corrosion resistance, chemical resistance, heat resistance, electrical insulation, and high adhesive strength. Of the various epoxy resins, the bisphenol A-type epoxy resin, which is produced via the polymerization of diglycidyl ether of bisphenol A (DGEBA) as shown in Figure 1-1, is mainly used in this thesis. The epoxy resin contains OH and -O- groups that can form hydrogen bonds with an adherend, including silica surfaces with hydroxyl groups.

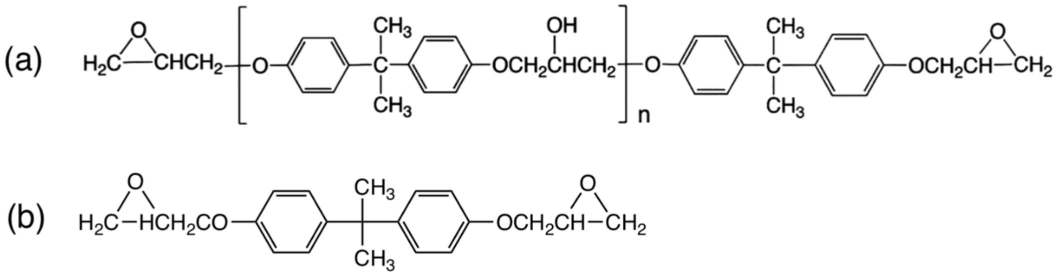

Figure 1-1. Structural formulae of (a) bisphenol A-type epoxy resin (polymer) and (b) its monomer, DGEBA.

1-2. Adhesion between the epoxy resin and silica surface

One common application of epoxy resins is the polymer matrix of fiber-reinforced plastic (FRP), which is a composite material made of synthetic polymers and fibers.[6] FRP is used commercially in the aerospace industry, the automotive industry, civil engineering and construction, and sporting goods. In these applications, the mechanical properties of the product are altered by the interfacial interaction between the adhesive and adherend. In chapter 2 and chapter 3, an epoxy resin/silica interface modeled on the structure of glass fiber reinforced plastic (GFRP) is theoretically investigated.

As shown in Figure 1-2, the silica surface is known to be terminated with silanol groups, which are assumed to be generated by the reaction with water in air.[7] From this, it can be inferred that hydrogen bonds are formed between the OH and -O- groups of the epoxy resin (Figure 1-1a) and the silanol groups on the silica surface. Previous studies have revealed H-bonding interactions between the epoxy resin and silica surface based on the optimized structure, and the H-bonding interactions were found to play an important role in improving the adhesive bond strength.[8]

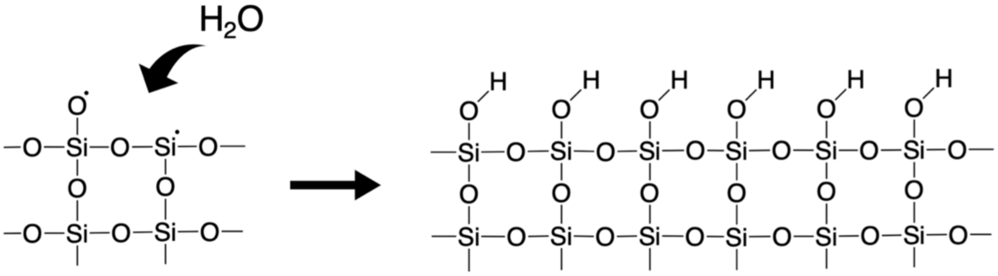

Figure 1-2. Schematic representation of the chemisorption process of water molecules on a bare silica surface. Dots denote surface dangling bonds.

1-3. Evaluation of energetic properties at the adhesive interface

In addition to structural features, the interaction energy (ΔE_{int}) is useful for evaluating interfacial interactions; ΔE_{int} is defined as follows:

$$\Delta E_{\mathrm{int}} = E_{12} - (E_1 + E_2), \qquad (1\text{-}1)$$

where E_{12} is the total energy of the adhesive–adherend complex; E_1 and E_2 are the energies of adhesive 1 and adherend 2, whose structures are maintained exactly the same as the adhesive–adherend complex. The structural deformation of the adhesion process is not taken into account, so ΔE_{int} corresponds to the pure interaction energy at the interface. On the other hand, the adhesion energy (ΔE_{ad}) is defined as follows:

$$\Delta E_{\mathrm{ad}} = (E_1^0 + E_2^0) - E_{12}, \tag{1-2}$$

where $E_1{}^0$ and $E_2{}^0$ are the energies of adhesive 1 and adherend 2, whose structures are optimized individually. This definition includes the structural deformation of both the adhesive and the adherend.

The difference between ΔE_{int} and ΔE_{ad} is called deformation energy (ΔE_{def}) and can be defined as follows:[9]

$$\Delta E_{\mathrm{def}} = (-\Delta E_{\mathrm{int}}) - \Delta E_{\mathrm{ad}} = (E_1 - E_1^0) + (E_2 - E_2^0), \tag{1-3}$$

where we multiply ΔE_{int} by –1 because of the difference in the ways ΔE_{int} and ΔE_{ad} are defined. Figure 1-3 shows the relationship between ΔE_{int}, ΔE_{ad}, and ΔE_{def}. ΔE_{int} is calculated as the stabilization energy of the adhesion (the process from b to a in Figure 1-3), while ΔE_{ad} represents the destabilization energy after the breakdown of the adhesive interface (the process from a to c in Figure 1-3). The direction of these processes producing ΔE_{int} and ΔE_{ad} is reversed. These three energies help ones to investigate adhesive phenomena at the molecular level. In chapter 2, the behavior of interfacial water molecules is elucidated from these energetic properties.

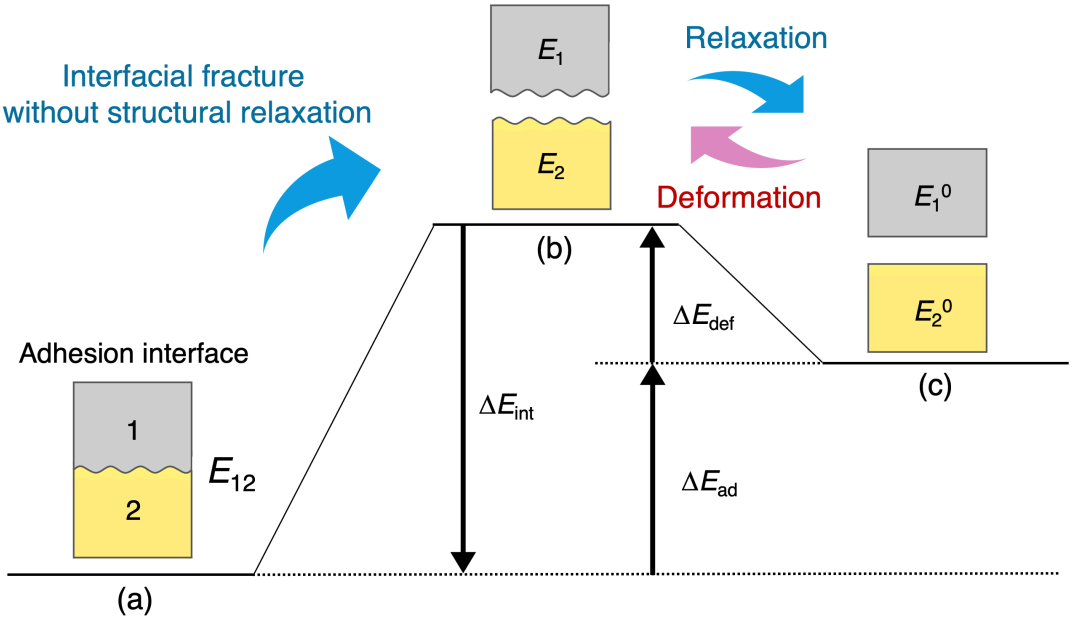

Figure 1-3. Diagram of the relationship between ΔE_{int}, ΔE_{ad}, and ΔE_{def}. (a) E_{12} is the total energy of the adhesive–adherend complex. (b) E_1 and E_2 are the energies of adhesive 1 and adherend 2, which maintain exactly the same structure as the adhesive–adherend complex while they are separated by infinity. (c) E_1^0 and E_2^0 are the energies of adhesive 1 and adherend 2, which are optimized (relaxed) during the separation.

In addition to the evaluation of ΔE_{int}, ΔE_{ad} and ΔE_{def}, there is another way to analyze energetic properties at the adhesive interface; ΔE_{int} can be decomposed into electrostatic contributions (ΔE_{es}), exchange repulsion (ΔE_{ex}), charge transfer (ΔE_{ct}), and dispersion (ΔE_{disp}) by using pair interaction energy decomposition analysis (PIEDA) as follows:[10,11]

$$\Delta E_{\mathrm{int}} = \Delta E_{\mathrm{es}} + \Delta E_{\mathrm{ex}} + \Delta E_{\mathrm{ct}} + \Delta E_{\mathrm{disp}}. \tag{1-4}$$

The interfacial interaction between the epoxy resin and silica surface has been clarified by using the PIEDA, leading us to the conclusion that the synergistic effects of the electrostatic and dispersion interactions are important in the OH-functionalized surfaces of the armchair edge of graphite and alpha-cristobalite.[8] Thus, decomposing ΔE_{int} may provide useful insight into the mechanisms of adhesive interactions that cannot be understood via structural features alone.

1-4. Evaluation of adhesion forces

The force resulting in adhesion can be calculated as follows:

$$F = \frac{\mathrm{d}E}{\mathrm{d}\Delta r}, \tag{1-5}$$

where Δr is the vertical displacement of the adhesive molecule from the position of stable equilibrium and E is the total energy of the adhesion complex. The values of Δr is varied in the direction perpendicular to a surface, and partial optimization is repeated at each step of Δr. The total energies obtained from the partial optimizations are plotted as a function of Δr as shown in Figure 1-4a. The energy versus Δr plots can be approximated by the Morse potential by using the least-squares method, where the Morse potential is written as follows:

$$E = D_\mathrm{e}(1 - \mathrm{e}^{-a\Delta r})^2, \tag{1-6}$$

where D_e is the depth of the potential well corresponding to binding energy, and a is a constant that determines the width of potential well. The smaller a is, the wider the potential well is.

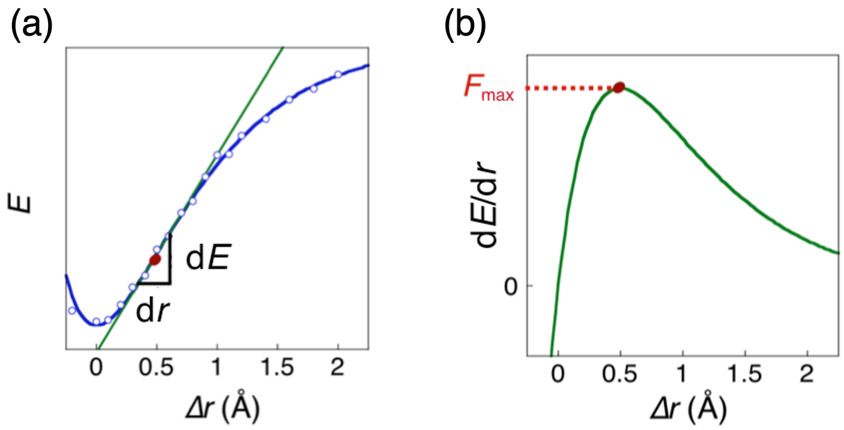

Figure 1-4. (a) Energy–displacement plots approximated by the Morse potential and (b) force–displacement curves with the maximum force $F_{\max}$ required for the interfacial failure at the molecular level.

According to eq (1-5), the differentiation of eq (1-6) by Δr gives a force–displacement curve as shown in Figure 1-4b. The maximum value of the force–displacement curve, denoted by $F_{\max}$, is a critical value required to break the interaction between adhesive and adherend at the adhesion interface. We assume $F_{\max}$ as the maximum force required for the interfacial failure at the molecular level. It should be noted that the interfacial models used in the present study do not consider a long polymer. In such models, it is difficult to consider the breaking of epoxy resin itself in the detachment process, i.e. cohesive failure, which is also essential in the breaking of real adhesive–adherend systems. The lack of the contribution from cohesive failure may cause a large difference between adhesive strengths measured experimentally and $F_{\max}$ estimated here. Nevertheless, the evaluation of $F_{\max}$ by using the models would provide a useful mechanistic insight into the role of adsorbed water molecules in the reduction of adhesion properties at the molecular level.

1-5. Glass transition temperatures

Glass transition temperature (T_g) is the temperature at which the polymer transfers from a rigid glass state to a soft rubber state. At this temperature there is sufficient free volume to allow molecules in the polymer backbone to move, so that rigid backbone relaxes and causes a transition from a solid polymer material to a quasi-liquid state.[12,13,14] Below the T_g, molecules can oscillate and vibrate around a fixed position creating a certain amount of free volume, which is dependent upon the temperature of the system. T_g plays an important role in determining the processing and performance properties such as heat resistance, durability, and adhesion of the polymer since heat capacity, coefficient of thermal expansion, and viscosity are affected by glass transition. Thus, T_gs of polymers are deeply related to adhesion properties.

However, it is difficult to uniquely determine T_g by experiment, and the differences between the reported values of T_g in literature can be very large. T_g is generally measured using Differential Scanning Calorimetry (DSC) or Dynamic Mechanical Thermal Analysis (DMTA).[12,13,15] Glass transition occurs over a relatively wide temperature range and depends on conditions such as measurement method, experimental period, and pressure under measurement. [12,16] T_g is also highly dependent on the structure of the polymer (crosslinking, chain stiffness), constitutive (additives, fillers, impurities), and conformation (stereo regularity).

Therefore, as shown in chapter 4, the chemoinfomatics approach of predicting polymer T_gs only from chemical structures may give us new insights into the investigation of polymer T_gs.

1-6. Significance of the theoretical study on adhesion for experimentalists

Experimentalists have been making great efforts to clarify every single adhesion phenomenon for the purpose of creating better adhesive applications for engineering. However, they sometimes face difficult situations with unmeasurable cases or difficult (time-consuming, complicated) cases to measure. For example, T_gs change depending on not only chemical structures of ingredients but also the cross-linking degrees, which are generally affected by the hardening process. Therefore, it is difficult to uniquely determine one T_g for one polymer. Fundamental theories that do not vary depending on the experimental conditions are demanded for the better understanding of adhesion systems and computational chemistry has great potential to provide clear answer from the atomistic point of view.

1-7. Overview of this thesis

In this thesis, we analyze adhesive properties of epoxy resin/silica interfaces on the basis of geometry-optimized structures and evaluate energies (ΔE_{int}, ΔE_{ad}, and ΔE_{def}). In chapter 2, we demonstrate that the adhesion properties are controlled by water molecules confined in the tight space between adhesive and adherend. In chapter 3, we reveal that synergistic effects of the electrostatic and dispersion interactions have important role in adhesive interaction by decomposing ΔE_{int} into ΔE_{es}, ΔE_{ex}, ΔE_{ct}, and ΔE_{disp}. These studies are carried out based on the *ab initio* calculations.

In chapter 4, we introduce the way how to create a predicting model of polymer T_gs including several types of epoxy resins by using chemoinfomatics approach. This work suggests a unified approach to predict T_gs of linear homo/hetero-polymers and cross-linked epoxy resins by machine-learning approaches based on descriptors of reagents undergoing polymerization, represented in a formal way such as to encompass all the three scenarios: linear homo- and heteropolymers, plus reticulated heteropolymers.

References

1. Ebnesajjad, S; Landrock, A. H. *Adhesives technology handbook,* 3rd ed.; William Andrew: London, 2015; pp 1–18.
2. *Fundamentals of adhesion*; Lee, L. H., Ed.; Springer Science+Business Media: New York, 1991.
3. *Handbook of Adhesion Technology*; da Silva, L. F. M., Öchsner, A., Adams, R. D. Eds.; Springer Science+Business Media: Berlin, Germany, 2011.
4. *Handbook of Adhesive Technology*; Pizzi, A., Mittal, K. L., Eds.; Marcel Dekker, Inc.: New York, 2003.
5. Petrie, E. M. Epoxy adhesives. In *Epoxy Adhesive Formulations*; McGraw-Hill Education:New York, 2005; Ch. 1, pp 1–26.
6. Petrie, E. M. Composites. In *Epoxy Adhesive Formulations*; McGraw-Hill Education:New York, 2005; Ch. 16.4, pp 378–381.
7. Klier, K.; Shen, J. H.; Zettlemoyer, A. C. Water on Silica and Silicate Surfaces. I. Partially Hydrophobic Silicas. *J. Phys. Chem.* **1973**, *77* (11), 1458–1465.
8. Yoshizawa, K.; Semoto, T.; Hitaoka, S.; Higuchi, C.; Shiota, Y.; Tanaka, H. Synergy of Electrostatic and van Der Waals Interactions in the Adhesion of Epoxy Resin with Carbon-Fiber and Glass Surfaces. *Bull. Chem. Soc. Jpn.* **2017**, *90* (5), 500–505.
9. Fedorov, D. G.; Kitaura, K. Subsystem Analysis for the Fragment Molecular Orbital Method and Its Application to Protein-Ligand Binding in Solution. *J. Phys. Chem. A* **2016**, *120* (14), 2218–2231.
10. Kitaura, K.; Morokuma, K. A new energy decomposition scheme for molecular interactions within the Hartree-Fock approximation. *Int. J. Quantum Chem.* **1976**, *10*, 325–340.
11. Fedorov, D. G.; Kitaura, K. Pair Interaction Energy Decomposition Analysis. *J. Comput. Chem.* **2006**, *28*, 222–237.
12. Sperling, L. H. *Introduction to Physical Polymer Science*, 4th ed; John Wiley & Sons, Inc. New Jersey, 2006.

13. Bicerano, J. *Prediction of Polymer Properties*, 3nd ed.; Marcel Dekker, Inc. New York, 2002.

14. Mattioni, B. E.; Jurs, P. C. Prediction of Glass Transition Temperatures from Monomer and Repeat Unit Structure Using Computational Neural Networks. *J. Chem. Inf. Comput. Sci.* **2002**, *42* (2), 232–240.

15. Cheremisinoff, N. P. *Polymer characterization: laboratory techniques and analysis*; Noyes Publications, New Jersey, 1996.

16. Krause, S.; Gormley, J. J.; Roman, N.; Shetter, J. A.; Watanabe, W. H. Glass Temperatures of Some Acrylic Polymers. *J. Polym. Sci. Part A* **1965**, *3* (10), 3573–3586.

Chapter 2. Molecular Understanding of the Adhesive Interactions between Silica Surface and Epoxy Resin: Effects of Interfacial Water

2-1. Introduction

Adhesion of synthetic polymers with organic and inorganic materials is widely applied to various industrial products.[1–5] Epoxy resin, one of the most common structural adhesives, is usually produced by the polymerization of diglycidylether of bisphenol A (DGEBA) shown in Figure 2-1. Epoxy resin adhesives are used for joining aluminum alloys for the structural skeleton of aircrafts and automobiles due to their advantages in lightweight and mechanical strength.[6] Important use of epoxy resin is polymer matrix of fiber-reinforced plastic (FRP), which is a composite material consisting of synthetic polymers and fibers. FRPs are commercially used in the aerospace and automotive industries, civil construction, and sports equipment.[7–13] In these applications, mechanical properties of the products are controlled by the interfacial interactions between the adhesive and the surface of adherend material.

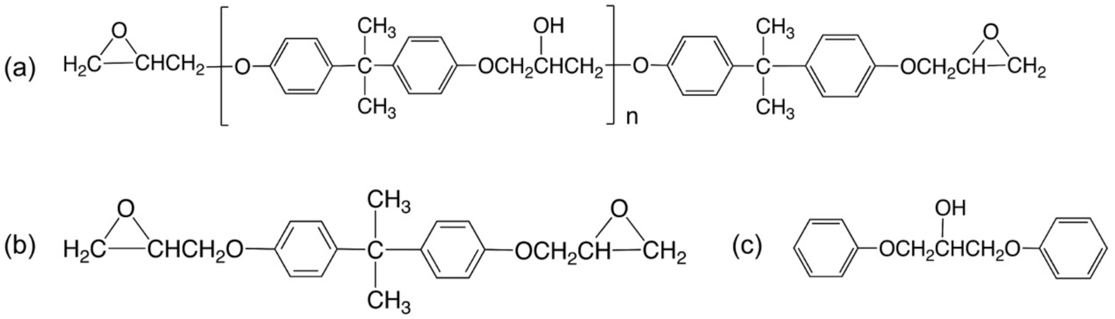

Figure 2-1. Chemical structures of (a) epoxy resin (polymerized DGEBA), (b) DGEBA monomer, and (c) a fragment of epoxy resin adopted as an adhesive model in the present study.

The origin of adhesion interaction has been discussed so far on the basis of various theories such as mechanical interlocking,[14,15] diffusion,[16] electrostatic interaction,[17–19] and adsorption.[1] According to widely accepted adsorption theory, adhesive and adherend can adhere through the forces working between the atoms in the interface region when appropriate intermolecular contact is achieved. Computational simulations at the molecular level will provide a better insight into the intermolecular forces acting at the adhesion interface. Recent computational studies have revealed the importance of hydrogen bonding in the adhesion of polymer–metal (metal oxide) interfaces and polymer–graphite interfaces under atmospheric or wet conditions.[20–30] We have theoretically investigated adhesion interactions in the epoxy resin–aluminum oxide interface[20,21] and the epoxy resin–graphite interface, [22,23] both of which are important from the viewpoint of industrial applications[31] and surface science.[32] In nature, marine mussels strongly adhere to minerals and metal oxide surfaces in seawater by using mussel adhesive proteins containing a catecholic amino acid, called Dopa (3,4-dihydroxyphenyl-L-alanine).[33,34] Experimental[35,36] and computational[27,28] studies on this biological adhesion have revealed that Dopa promotes the strong adhesion under wet conditions through the hydrogen-bonding interaction between the hydroxyl (OH) groups of catechol and the hydrophilic target surface.

Glass-fiber-reinforced plastic (GFRP) is a composite material, in which glass fibers are impregnated in matrix made of synthetic polymers such as epoxy resin. GFRP offers lots of advantages over traditional materials, for instance, a high strength-to-weight ratio, non-magnetic, and chemical/corrosion resistance.[8,13] Although significant experimental efforts have been devoted to the improvement of adhesion properties of the interface between synthetic polymers and glass surfaces,[8,13,37–39] there still remains a lack of detailed understanding on the mechanism of adhesion between them at the molecular level. In computational analyses of glass surfaces, the structure of amorphous silica is often modeled with that of cristobalite.[27,28,40–42] Under normal conditions, the silica surface chemisorbs water molecules to form surface OH groups.[43–48] The hydrophilic silica surface covered with OH groups attracts additional water molecules to form a network of hydrogen bonds on the surface.[43,46,49] It is empirically known that water vapor in moist air decreases adhesion properties of the composites.[13] Weak boundary layer of the physisorbed water hinders the intermolecular contact between polymers and adherend surfaces.[33] Collins and coworkers measured the concentration of water monolayer on hydroxylated mesoporous silica surfaces by gravimetric analysis.[49] Figure 2-2 shows a schematic drawing of silica surface under normal conditions. In the context of adsorption theory for adhesion phenomena, we expect that the hydrogen-bonding interactions between the surface OH groups and the oxygen-containing functional groups of epoxy resin play a pivotal role in the adhesion of silica surface and epoxy resin. We previously showed that the hydrogen bonds between OH/COOH-functionalized graphite surfaces and oxygen-containing functional groups of epoxy resin are mainly responsible for the adhesion interactions in carbon fiber/epoxy resin systems.[22, 23] For a better modeling of the interfacial adhesion between polymer adhesives and hydrophilic adherend surfaces, it is essential to consider water molecules located in the adhesion interface under atmospheric conditions. There are quite limited computational studies that treated the moisture-induced weakening of adhesion at the molecular level.[20,21,30,50] Ogata and Takahashi have analyzed the moist-induced reduction of adhesion strength between hydroxylated aluminum oxide surface and polymer of epoxy resin in the presence of interfacial water molecules using the hybrid quantum-classical method.[30] Their large-scale calculations reasonably reproduced that the shear strength of the interfacial adhesion is significantly reduced as a degree of moisture content increases. We previously performed periodic DFT calculations to shed light on the molecular mechanism of the adhesion between epoxy resin and aluminum surface, where the surface was modeled by aluminum oxide covered with OH groups.[20,21] Calculated adhesion energies and forces suggest that water molecules adsorbed on hydrophilic aluminum oxide surface have significant effects on the interactions at the adhesion interface.

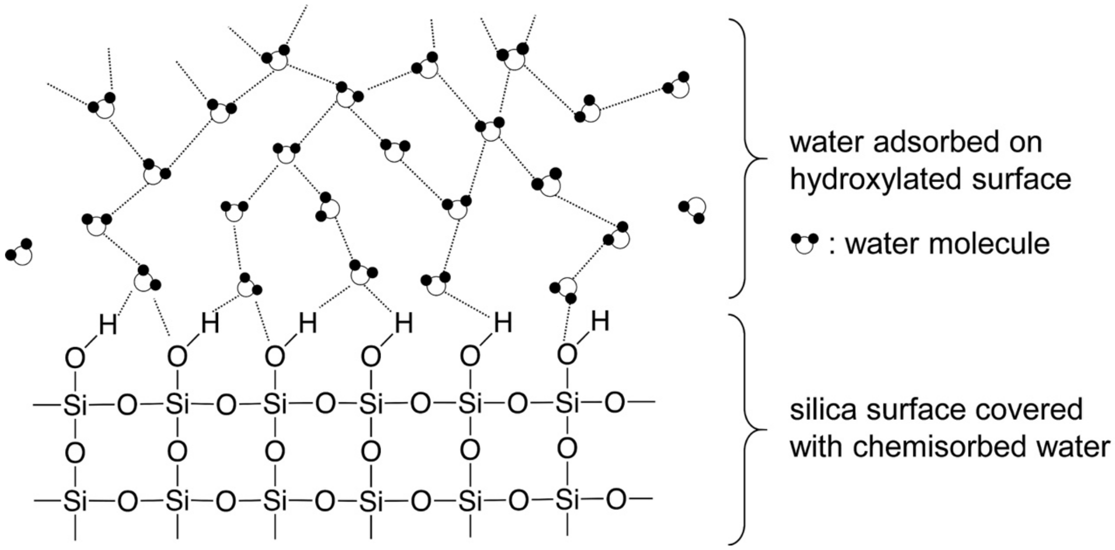

Figure 2-2. Schematic representation of a plausible surface structure of silica under normal conditions.

In the present study, we theoretically investigate the adhesion interface between glass fiber and epoxy resin by constructing interfacial models under normal conditions. To clarify intermolecular interactions working at the adhesion interface, periodic DFT calculations are applied to slab models consisting of a fragment of epoxy resin and hydrophilic silica surfaces with or without adsorbed water molecules. Effects of water on the interfacial adhesion are evaluated on the basis of geometry-optimized structures, adhesion energies, and adhesion forces. We demonstrate that the adhesion properties are controlled by structural flexibility of the network of hydrogen bonds formed in the interface region as well as structural deformation of the hydrogen-bonding network of water molecules confined in the tight space between adhesive and adherend.

2-2. Method details

2-2-1. Modeling of silica surfaces

We modeled the surface of glass fiber (amorphous silica), the reinforcing material of GFRP, by cleaving the bulk structure of α-cristobalite according to previous computational studies on hydroxylated silica surfaces.[23,27,28] A periodic model of the silica surface was prepared by cleaving the bulk structure of α-cristobalite on the (0 0 1) surface, and a vacuum layer of 40 Å thickness was added to build a slab model. The unit cell contains 6 Si atoms and 12 O atoms, its lattice parameters being a = 4.978 Å, b = 4.978 Å, and c = 49.679 Å. To realize hydroxylated silica surface, two water molecules were dissociatively adsorbed on the top and bottom layers of the slab. As a result, the surface contains geminal silanol groups (two OH groups attached to each Si atom) and the density of surface silanol groups is 4.0 per nm^2. This value is close to a typical density on amorphous silica, 5 OH per nm^2.[45] After this treatment, the hydroxylated silica surface has one surface OH group and one H atom on a neighboring O atom of the Si–O–Si bridge on both sides. As a result, the unit cell of the hydroxylated silica surface involves 24 atoms, $Si_6O_{12}•2H_2O$. The structure of the hydroxylated silica surface was fully optimized with periodic DFT calculations using the CASTEP software package of Materials Studio 6.1.[51] The functional used here is the Perdew-Burke-Ernzerhof form of generalized gradient approximation (GGA-PBE)[52] with dispersion corrections by Grimme.[53] Recently we applied energy decomposition analysis for cluster models of epoxy resin–graphite and epoxy resin–silica interfacial systems and demonstrated the importance of both electrostatic and dispersion interactions in the adhesion of epoxy resin and hydroxylated silica surface.[23] It is noted that the combination of PBE and Grimme's dispersion correction can sometimes have a rather underwhelming performance for systems where hydrogen bonding is dominant.[54] Actually, we confirmed that this combination gave smaller absolute values of adhesion energies than the combination of PBE and the Tkatchenko-Scheffler's correction;[55] however, our conclusions on the reduction of adhesion in the presence of surface water molecules were unchanged. The plane-wave basis set with a cutoff energy of 340 eV was applied for the system with the periodic boundary conditions. Electron-ion interactions were treated with ultrasoft pseudopotentials. A *k*-point set of 3 × 3 × 1 was used.

Finally, as shown in Figure 2-3a, a 2 × 2 supercell of unit cell was prepared for the construction of adhesion interfacial models. The lattice parameters of the supercell are a = 9.956 Å, b = 9.956 Å, and c = 49.679 Å. Water-adsorbed models of hydroxylated silica surface were prepared by using molecular dynamics (MD) simulations with the COMPASS force field,[56–58] a classical force field with parameters derived from *ab initio* calculations optimized for condensed phase applications, implemented in the Forcite software package of Materials Studio 6.1.[51] The COMPASS force field is applicable for describing molecular systems in which hydrogen bonding interactions play an important role.[59] In all the MD simulations, the system was kept at a constant temperature (300 K) by using NVT ensemble with the Nosé-Hoover thermostat. Total dynamics time was set to be 100 ps with a time step of 1 fs. The number of water molecules absorbed on hydroxylated silica surface was determined based on measurements of water monolayer on mesoporous silicas by Collins and coworkers.[49] They reported that water monolayer has a concentration of 7.68 ± 0.30 μmol H_2O/m^2. In the present small surface model, the 5-water model (8.38 μmol H_2O/m^2) correspond to the experimental value. To assess the impact of the thickness of surface water layer in the adhesion interaction, we considered two models for water-absorbed silica surface involving 5 and 10 water molecules, as shown in Figure 2-3b and 3c. For each model, the water molecules were randomly located above the hydroxylated silica surface, and then 100-ps dynamics were performed at 300 K. Consequently, we employed three models of the hydroxylated silica surface with and without adsorbed water molecules in Figure 2-3 for subsequent DFT calculations on adhesive–adherend complexes.

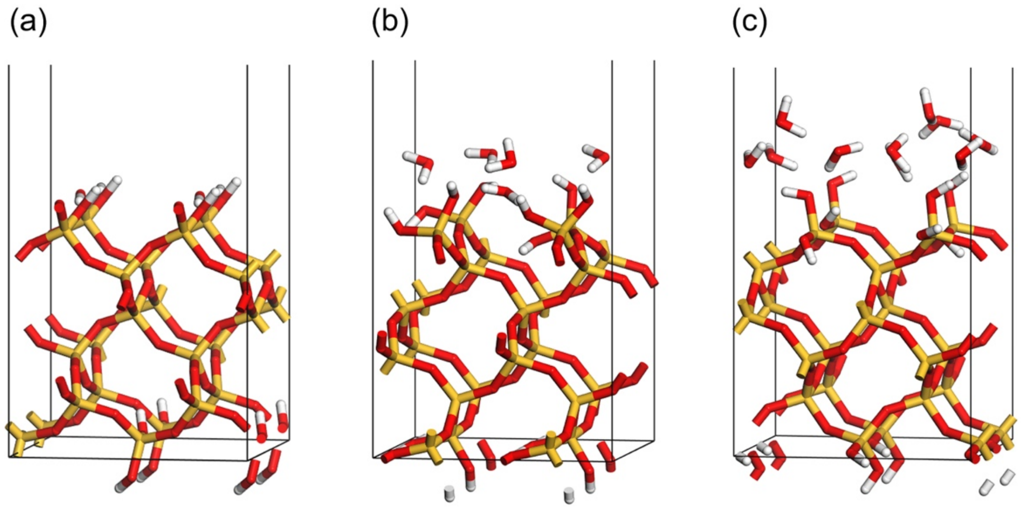

Figure 2-3. Three models of hydroxylated silica surface. (a) The surface without adsorbed water molecules (dry model), (b) with 5 adsorbed water molecules (5-water model), and (c) with 10 adsorbed water molecules (10-water model).

2-2-2. Geometry optimization of adhesive–adherend complexes

In the present study, epoxy resin adhesive was modeled by a fragment molecule shown in Figure 2-1c. The structure of the fragment is the same as that used in previous studies,[20–22] containing two benzene rings, two ether groups, and one OH group. The three slab models with or without absorbed water molecules were constructed from the hydroxylated silica surface models prepared in the former section and the fragment of epoxy resin. The fragment was randomly located above the silica surface, and then MD simulations were performed with a dynamics time of 100 ps at 300 K. We confirmed that thermal equilibrium of NVT ensemble was achieved after 100 ps-simulations. Twenty trajectories for each slab model were obtained for the preparation of twenty initial structures for the following DFT calculations. In all the trajectory calculations, we observed the formation of hydrogen bond network among the surface OH groups, the oxygen-containing groups of the epoxy resin fragment, and the adsorbed water molecules. Excessive vacuum layer of 20 Å thickness was cut from the final supercell geometry of the MD simulation to rebuild a smaller unit cell for the following DFT calculations. The lattice parameters of the rebuild supercell are a = 9.956 Å, b = 9.956 Å, c = 29.679 Å. The 20 MD-based structures of each slab model were optimized with the GGA-PBE method with plane-wave energy cutoff of 340 eV and a 1 × 1 × 1 k-point set. At the optimized geometries, single-point energy calculations with plane-wave energy cutoff of 380 eV and a 2 × 2 × 1 k-point set were carried out. In this optimization process, the surface Si atoms, the O (OH) groups connecting to them, water molecules, and the fragment of epoxy resin were allowed to relax. Finally, the lowest-energy structure chosen from twenty candidates was adopted as an adhesion interfacial model for further analyses.

2-2-3. Calculation of adhesion energies

The adhesion energy, ΔE_{ad}, which is the net energy change in the adhesion process, can be calculated as follows:

$$\Delta E_{\mathrm{ad}} = E^{\mathrm{complex}}_{(\mathrm{adhesive+adherend})} - (E^{\mathrm{adhesive}}_{\mathrm{adhesive}} + E^{\mathrm{adherend}}_{\mathrm{adherend}}) \qquad (2\text{-}1)$$

where $E^{\mathrm{complex}}_{(\mathrm{adhesive+adherend})}$ is the total energy of the adhesive–adherend complex and $E^{\mathrm{adhesive}}_{\mathrm{adhesive}}$ and $E^{\mathrm{adherend}}_{\mathrm{adherend}}$ are the energies of the fragment of epoxy resin and the hydroxylated silica surface, respectively. The geometries of the epoxy resin fragment and silica surface are separately optimized in the calculation of ΔE_{ad}. In this definition, a negative value of ΔE_{ad} denotes an exothermic adhesion process. Since the adhesion process results in the structural deformation of both adhesive and adherend, ΔE_{ad} can be associated with measurable energy change in the adhesion process. In order to estimate the strength of the adhesion interaction independent of the structural deformation,[60] we define the adhesion interaction energy, E_{int}, according to the following equation:

$$E_{\mathrm{int}} = E^{\mathrm{complex}}_{\mathrm{adhesive}} + E^{\mathrm{complex}}_{\mathrm{adherend}} - E^{\mathrm{complex}}_{(\mathrm{adhesive+adherend})} \qquad (2\text{-}2)$$

where $E_{\mathrm{adhesive}}^{\mathrm{complex}}$ and $E_{\mathrm{adherend}}^{\mathrm{complex}}$ are the energies of adhesive and adherend whose geometries are fixed to those in the complex, respectively. The adhesion interaction energy can be interpreted as the energy necessary to break all the interactions between adhesive and adherend. We can use E_{int} as a theory-based indicator of the strength of adhesion interaction. A larger positive value of E_{int} corresponds to stronger interaction between adhesive and adherend, and E_{int} is opposite in sign to ΔE_{ad} by definition. The structural deformation destabilizes the adhesion system, and therefore the absolute value of ΔE_{ad} is always smaller than that of E_{int}. The relationship between ΔE_{ad} and E_{int} is described as follows:

$$-\Delta E_{\mathrm{ad}} = E_{\mathrm{int}} - E_{\mathrm{def}} \qquad (2\text{-}3)$$

where the deformation energy E_{def} is the energy loss derived from the structural deformation of the adhesive and the adherend in the adhesion process. The value of E_{def} obtained for the adhesive–adherend complex can be separated into two partial deformation energies derived from adhesive and adherend, $E_{\mathrm{def(adhesive)}} = E_{\mathrm{adhesive}}^{\mathrm{complex}} - E_{\mathrm{adhesive}}^{\mathrm{adhesive}}$ and $E_{\mathrm{def(adherend)}} = E_{\mathrm{adherend}}^{\mathrm{complex}} - E_{\mathrm{adherend}}^{\mathrm{adherend}}$.

2-2-4. Evaluation of adhesion forces

The force resulting in adhesion can be calculated as follows:

$$F = \frac{\mathrm{d}E}{\mathrm{d}\Delta r} \qquad (2\text{-}4)$$

where Δr is the vertical displacement of the adhesive molecule from the position of stable equilibrium and E is the total energy of the adhesion complex. The values of Δr was varied in the direction perpendicular to the α-cristobalite (0 0 1) surface from –0.4 to 2.0 Å at an interval of 0.2 Å, and partial optimization was repeated at each step of Δr. In the partial optimization, the surface Si atoms, the O(H) groups connecting to them, the adsorbed water molecules, and the OH group in the fragment of epoxy resin were allowed to relax. We applied the same procedure for the three interfacial models to investigate how the wetting of silica surface influences the adhesion interaction. The total energies obtained from the partial optimizations were plotted as a function of Δr. The energy versus Δr plots were approximated by the Morse potential by using the least-squares method in the range from –0.4 to 2.0 Å, where the Morse potential is written as follows:

$$E = D_\mathrm{e}(1 - \mathrm{e}^{-a\Delta r})^2 \qquad (2\text{-}5)$$

where D_e is the depth of the potential well corresponding to binding energy, and a is a constant that determines the width of potential well. The smaller a is, the wider the potential well is. According to eq 2-4, the differentiation of eq 2-5 by Δr gives a force–displacement curve. The maximum value of the force–displacement curve, denoted by F_max, is a critical value required to break the interaction between adhesive and adherend at the adhesion interface. We assume F_max as the maximum force required for the interfacial failure at the molecular level. It should be noted that the interfacial models used in the present study do not consider a long polymer. In such models, it is difficult to consider the breaking of epoxy resin itself in the detachment process, i.e. cohesive failure, which is also essential in the breaking of real adhesive–adherend systems. The lack of the contribution from cohesive failure may cause a large difference between adhesive strengths measured experimentally and F_max estimated here. Nevertheless, the evaluation of F_max by using the models would provide a useful mechanistic insight into the role of adsorbed water molecules in the reduction of adhesion properties at the molecular level.

2-3. Results and discussion

2-3-1. Interfacial structures and energetic properties of adhesive–adherend complexes

Figure 2-4 shows the lowest-energy structures of the three models of adhesion interface between epoxy resin and silica surface. For the dry model in Figure 2-4(a), the OH groups on the silica surface form hydrogen bonds with the OH and ether groups of the fragment of epoxy resin, where the surface OH groups serve as both donor and acceptor of hydrogen bonding. For the two models involving adsorbed water molecules in Figure 2-4(b) and (c), on the other hand, the water molecules are located in the space between the silica surface and epoxy resin to form the hydrogen bond network. While the direct hydrogen-bonding interaction between the adhesive and adherent remains in the 5-water model in Figure 2-4(b), the surface OH groups are fully occupied by the adsorbed water molecules in the 10-water model in Figure 2-4(c). The lowest-energy structures of the 5- and 10-water models could imply that the strength of bonding interaction between the epoxy resin and silica surface is comparable with that between the epoxy resin and the water molecules.

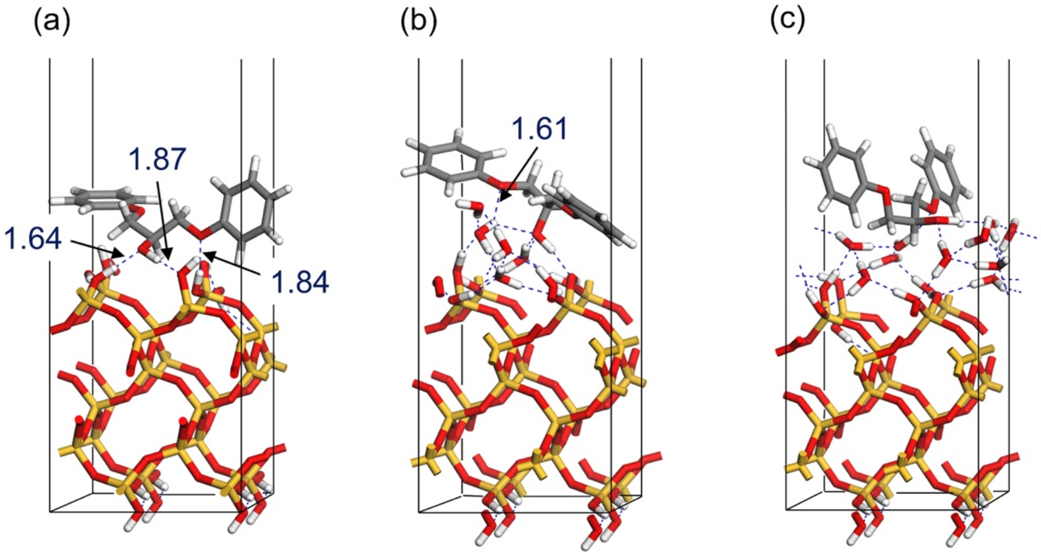

Figure 2-4. The lowest-energy structures of (a) dry model, (b) 5-water model, and (c) 10-water model. Blue dashed lines indicate hydrogen-bonding interactions, where the O···H distance less than 2.5 Å is regarded as a hydrogen bond.

Table 2-1 summarizes energetic properties ΔE_{ad} and E_{int} obtained for the optimized structures of the three adhesion models in accordance with eqs 2-1 and 2-2 in the former section. The adhesion energies ΔE_{ad} at the adhesion interface between the epoxy resin and the silica surface are calculated to be –145.7 kJ mol^{-1} for the dry model, –113.0 kJ mol^{-1} for the 5-water model, and –92.0 kJ mol^{-1} for the 10-water model. Since ΔE_{ad} can be associated with measurable energy change in the adhesion process, ΔE_{ad} of each model was also given in units of mJ m^{-2} in Table 2-1. The presence of water molecules at the adhesive interface significantly reduces ΔE_{ad}, which correspond to the heat of adhesion that is experimentally measurable. On the other hand, the adhesion interaction energies E_{int} seem to be independent of the number of adsorbed water molecules; 168.1 kJ mol^{-1} for the dry model, 169.0 kJ mol^{-1} for the 5-water model, and 173.7 kJ mol^{-1} for the 10-water model. The E_{int} values obtained for the present interfacial models would be interpreted in two ways: (1) Interfacial water does not influence the strength of the adhesion interaction between the epoxy resin and silica surface, and (2) the strength of the adhesion interaction between the epoxy resin and the silica surface is very similar to that between the epoxy resin and water. The latter can be associated with the lowest-energy structure of the 5-water model, in which both direct and indirect hydrogen bonding interactions were observed between the epoxy resin and the OH groups on the silica surface. The different tendency in ΔE_{ad} and E_{int} is understood by considering the structural deformation of the adhesive and adherend upon formation of the adhesive–adherend complex. Table 2-1 summarizes the deformation energy E_{def} and its components $E_{\mathrm{def(adhesive)}}$ and $E_{\mathrm{def(adherend)}}$ obtained for the three models. The energy loss derived from the epoxy resin, $E_{\mathrm{def(adhesive)}}$, is 9.1 kJ mol^{-1} for the dry model, 21.7 kJ mol^{-1} for the 5-water model, and 27.0 kJ mol^{-1} for the 10-water model. A larger part of the energy loss during the adhesion comes from the silica surface, particularly from the adsorbed water molecules; $E_{\mathrm{def(adherend)}} = 13.3$ kJ mol^{-1} for the dry model, 34.3 kJ mol^{-1} for the 5-water model, and 57.4 kJ mol^{-1} for the 10-water model. Consequently, confinement of the water molecules in the tight space between the adhesive and adherend should result in a significant difference between the magnitude of ΔE_{ad} and E_{int}. Since the structure of the hydroxylated silica surface is nearly unchanged in the three models, the contribution of the adsorbed water molecules to $E_{\mathrm{def(adherend)}}$ can be estimated to be 21.0 kJ mol^{-1} for the 5-water model and 41.4 kJ mol^{-1} for the 10-water model. Thus, we can roughly evaluate that each water molecule reduces the strength of the adhesion interaction between the silica surface and epoxy resin by ~4 kJ mol^{-1}. From the energetic point of view, the hydrogen-bonding network of the interfacial water should play a key role in the reduction of the adhesion between the hydroxylated silica surface and epoxy resin.

Table 2-1. Energetic properties of the adhesion between silica surface and epoxy resin

Model	ΔE_{ad}		E_{int}	E_{def}	$E_{\mathrm{def(adhesive)}}$	$E_{\mathrm{def(adherend)}}$
	/kJ mol^{-1}	mJ m^{-2}	/kJ mol^{-1}	/kJ mol^{-1}	/kJ mol^{-1}	/kJ mol^{-1}
Dry	-145.7	-244.2	168.1	22.4	9.1	13.3
5-water	-113.0	-189.3	169.0	56.0	21.7	34.3
10-water	-92.0	-154.1	173.7	81.7	27.0	54.7

2-3-2. Adhesion forces acting at the silica surface/epoxy resin interface

Figure 2-5 shows energy–displacement plots for the three interfacial models. Obtained fitting parameters D_e and a are listed in Table 2-2. The plots in the range from –0.4 to 2.0 Å were nicely approximated by the Morse potential. The value of D_e representing the depth of the approximated curve is 171.4 kJ mol^{-1} for the dry model, which is very close to those of the wet surface models, 183.8 kJ mol^{-1} for the 5-water model and 186.0 kJ mol^{-1} for the 10-water model. The trend of D_e for the three models resembles in that of E_{int} in Table 2-1. It is noteworthy that the detachment of epoxy resin from the water-adsorbed silica surfaces shows a gradual change in energy compared to the dry surface. Moreover, the increase in the number of water molecules at the adhesion interface emphasizes a slow rising of the total energy toward the dissociation limit. In the detachment process, the water molecules in the interfacial region are able to rearrange their positions so as to optimize the network of hydrogen bonding connecting the adhesive and adherend. Thus, the hydrogen-bonding network of the interfacial water molecules can stabilize the adhesive–adherend complex in the detachment process. Actually, the detachment process in the dry model exhibits that the bonding interactions between the hydroxylated silica surface and the epoxy resin are rapidly diminished with an increase in Δr. The gradual increase in energy in the detachment is reflected in parameter a that controls the width of the approximated curve. As shown in Table 2-2, the 10-water model gives a smaller value of a (0.61 Å^{-1}) than the dry model (0.96 Å^{-1}) and the 5-water model (0.70 Å^{-1}).

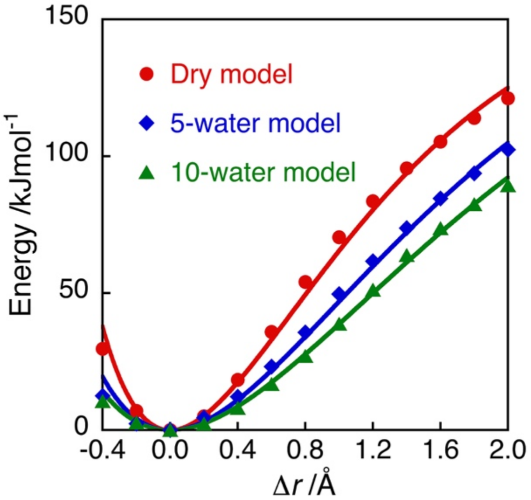

Figure 2-5. Energy–displacement plots for the dry and wet surface models and the potential energy curves fitted by the Morse potential. The fitting parameters are listed in Table 2-2.

Figure 2-6 presents force–displacement curves given by the first derivative of the approximated energy–displacement curves. Table 2-2 summarizes the maximum adhesion force $F_{\max}$ and the displacement Δr_F that gives the maximum force $F_{\max}$. The values of $F_{\max}$ (Δr_F) are calculated to be 1.37 nN (0.72 Å) for the dry model, 1.07 nN (0.98 Å) for the 5-water model, and 0.94 nN (1.14 Å) for the 10-water model. The interfacial water molecules significantly influence both $F_{\max}$ and Δr_F. The increase in the number of water molecules decreases $F_{\max}$ and increases Δr_F. The values of $F_{\max}$ and Δr_F equal to $(1/2)aD_e$ and $-\log_e(1/2)/a = 0.693/a$ in accordance with eqs 2-4 and 2-5, and therefore both $F_{\max}$ and Δr_F depend on only parameter a because the values of D_e are almost similar in the three interfacial models. In the wet surface models, the gradual increase in energy in the detachment process is directly related to the smaller values of $F_{\max}$, because the adhesion force is defined as the gradient of potential energy. While the hydrogen-bonding network provided by the interfacial water molecules always stabilizes the adhesive–adherend complex during the detachment, it is interesting that this stabilization leads to the decrease of adhesion force.

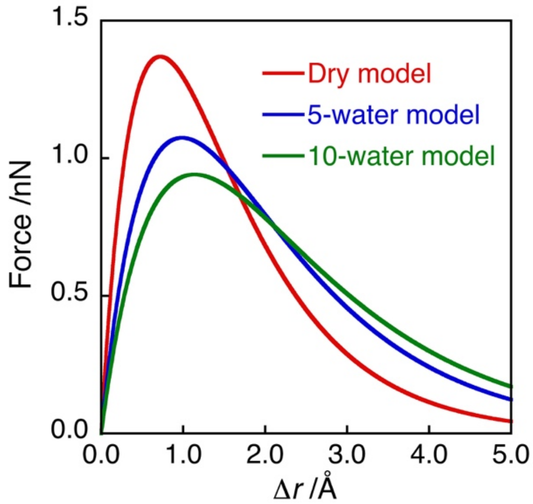

Figure 2-6. Force–displacement curves for the dry and wet surface models.

Table 2-2. Theoretical adhesion properties and fitting parameters for the dry and wet surface models

Model	F_{max} /nN	Δr_{F} /Å	D_{e} /kJ mol^{-1}	a /Å^{-1}	S_{ad} /GPa
Dry	1.37	0.72	171.4	0.96	1.38
5-water	1.07	0.98	183.8	0.70	1.08
10-water	0.94	1.14	186.0	0.61	0.95

To compare F_{max} with the adhesion strength as a macroscopic property, we converted F_{max} to the maximum adhesion stress (S_{max}), which can be calculated from F_{max} and the lattice area (A_{lattice}) as follows:

$$S_{\mathrm{max}} = \frac{F_{\mathrm{max}}}{A_{\mathrm{lattice}}} \qquad (6)$$

where $A_{\mathrm{lattice}} = 9.912 \times 10^{-19}$ m^{-2}. In the models employed here, S_{max} corresponds to the maximum stress required for the interfacial failure of the adhesive–adherend complexes. The values of S_{max} are 1.38 GPa for the dry model, 1.08 GPa for the 5-water model, and 0.95 GPa for the 10-water model. These values are one or two order of magnitude larger than the adhesion strength (17.4 MPa) measured by tensile test.[38] The adhesion strength measured for real adhesion systems can be significantly reduced by various factors, such as surface asperity, impurity contamination, internal stress, blister formation, and solvent retention. In the present study, we have modeled the adhesion interfaces without any consideration of these real factors in experiment. Moreover, in the present computational models we could not reasonably consider the cohesive failure of the adhesion system, which is the breaking of polymer structure of adhesive. Although measured forces significantly depend on strain rate in general, it is difficult to take such dynamic effects into account from the limit of the present DFT calculations. One of the most important factors that can reduce adhesion strength is considered to be heat effects, which are not taken into account within the framework of the present quantum mechanical treatment. In such cases calculated adhesion stresses are usually overestimated by one or two orders of magnitude.[20–21] However, we think that the adhesion properties obtained with the interfacial models would provide valuable mechanistic insight into the reduction of adhesion in the presence of interfacial water at the molecular level.

2-4. Conclusion

For a better understanding of adhesion phenomena at the molecular level, we have focused on the interfacial adhesion between silica surface and epoxy resin in the presence of interfacial water. Periodic DFT calculations were applied to the adhesion interfaces modeled by slab models composed of a hydroxylated silica surface, water molecules adsorbed on the surface, and a fragment of epoxy resin. Three interfacial models in the presence or absence of the adsorbed water molecules (dry, 5-water, and 10-water models) were prepared to clarify how moisture in the air influences adhesion properties.

Energetic properties of the adhesion at the silica surface/epoxy resin interface were evaluated with two indices, the adhesion energy (ΔE_{ad}) and the adhesion interaction energy (E_{int}), where the former can correspond to the measureable energy change in the adhesion process and the latter can be interpreted as the interaction energy independent of structural deformation upon adhesion. Calculated values of ΔE_{ad} are significantly smaller than E_{int} in the wet models involving adsorbed water molecules, and the deformation energy (E_{def}) defined as the difference between ΔE_{ad} and E_{int} increases with increasing the number of the water molecules. It is also notable that the value of E_{int} calculated for the dry model is very close to those for the wet surface models. These results indicate that water molecules confined in a tight space between the adhesive and the adherend should cause an energy loss derived from the deformation of the hydrogen-bonding network in the interfacial region.

Energy changes during detachment of the epoxy resin from the silica surface were nicely approximated by the Morse potential, and the maximum values of the theoretical adhesion force (F_{max}) were estimated based on the approximated curves. The increase in the number of adsorbed water molecules effectively decreases F_{max} because the water molecules can rearrange their positions in a wider space formed in the detachment process so as to optimize the hydrogen-bonding network. The gradual energy change in the detachment process results in the smaller values of F_{max} obtained for the wet surface models. In conclusion, we theoretically shed light on the molecular mechanism of the reduction of adhesion between silica surface and epoxy resin under moist conditions. Water vapor in the air can exert a negative influence on the adhesion properties through the structural deformation of the hydrogen-bonding network of water molecules at the adhesion interface as well as the structural flexibility of the hydrogen-bonding network in the detachment process.

References

1. Kinloch, A. J. The Science of Adhesion. *J. Mater. Sci.* **1980**, *15*, 2141–2166.
2. Wake, W. C. *Adhesion and the Formulation of Adhesives*, 2nd ed.; Applied Science Publishers, London, 1982.
3. Fourche, G. An Overview of the Basic Aspects of Polymer Adhesion. Part I: Fundamentals. *Polym. Eng. Sci.***1995**, *35*, 957–967.
4. Fourche, G. An Overview of the Basic Aspects of Polymer Adhesion. Part II: Application to Surface Treatments. *Polym. Eng. Sci.* **1995**, *35*, 968–975.
5. Cognard, J. Some Recent Progress in Adhesion Technology and Science. *C. R. Chim.* **2006**, *9*, 13–24.
6. Brockmann, W.; Hennemann, O.-D.; Kollek, H.; Matz, C. Adhesion in Bonded Aluminium Joints for Aircraft Construction. *Int. J. Adhes. Adhes.* **1986**, *6*, 115–143.
7. Simon, R.; Prosen, S. P.; Duffy, J. Carbon Fiber Composites. *Nature* **1967**, *213*, 1113−1114.
8. Ishida, H.; Koenig, J. L. The Reinforcement Mechanism of Fiber-Glass Reinforced Plastics Under Wet Conditions: A Review. *Polym. Eng. Sci.* **1978**, *18*, 128–145.
9. Fitzer, E.; Geigl, K.-H.; Hüttner, W.; Weiss, R. Chemical Interaction between the Carbon Fibre Surface and Epoxy Resin. *Carbon* **1980**, *18*, 389–393.
10. Park, S.-J.; Kim, B.-J. Role of Acidic Functional Groups of Carbon Fiber Surface in Enhancing Interfacial Adhesion Behavior. *Mater. Sci. Eng. A* **2005**, *408*, 269–273.
11. Dai, Z.; Shi, F.; Zhang, B.; Li, M.; Zhang, Z. Effect of Sizing on Carbon Fiber Surface Properties and Fibers/Epoxy Interfacial Adhesion. *Appl. Surf. Sci.* **2011**, *257*, 6980–6985.
12. Deng, S.; Zhou, X.; Fan, C.; Lin, Q.; Zhou, X. Release of Interfacial Thermal Stress and Accompanying Improvement of Interfacial Adhesion in Carbon Fiber Reinforced Epoxy Resin Composites: Induced by Diblock Copolymers. *Composites Part A* **2012**, *43*, 990–996.
13. Sathishkumar, T. P.; Satheeshkumar, S.; Naveen, J. Glass Fiber-Reinforced Polymer Composites-a Review. *J. Reinf. Plast. Compos.* **2014**, *33*, 1258–1275.
14. McBain, J. W.; Hopkins, D. G. On Adhesives and Adhesive Action. *J. Phys. Chem.* **1925**, *29*, 188–204.
15. Packham, D. E.; Johnston, C. Mechanical Adhesion: Were McBain and Hopkins Right? An

Empirical Study. *Int. J. Adhes. Adhes.* **1994**, *14*, 131–135.

16. Voyutskii, S. S.; Vakula, V. L. The Role of Diffusion Phenomena in Polymer-to-Polymer Adhesion. *J. Appl. Polym. Sci.* **1963**, *7*, 475–491.
17. Derjaguin, B. V.; Smilga, V. P. Electronic Theory of Adhesion. *J. Appl. Phys.* **1967**, *38*, 4609–4616.
18. von Harrach, H. G.; Chapman, B. N. Charge Effects in Thin Film Adhesion. *Thin Solid Films* **1972**, *13*, 157–161.
19. Roberts, A. D.; Allen, K. W. *Adhesion*, Applied Science Publishers, London, **1977**.
20. Semoto, T.; Tsuji, Y.; Yoshizawa, K. Molecular Understanding of the Adhesive Force between a Metal Oxide Surface and an Epoxy Resin. *J. Phys. Chem. C* **2011**, *115*, 11701–11708.
21. Semoto, T.; Tsuji, Y.; Yoshizawa, K. Molecular Understanding of the Adhesive Force between a Metal Oxide Surface and an Epoxy Resin: Effects of Surface Water. *Bull. Chem. Soc. Jpn.* **2012**, *85*, 672–678.
22. Semoto, T.; Tsuji, Y.; Tanaka, H.; Yoshizawa, K. Role of Edge Oxygen Atoms on the Adhesive Interaction between Carbon Fiber and Epoxy Resin. *J. Phys. Chem. C* **2013**, *117*, 24830–24835.
23. Yoshizawa, K.; Semoto, T.; Hitaoka, S.; Higuchi, C.; Shiota, Y.; Tanaka, H. Synergy of Electrostatic and van der Waals Interactions in the Adhesion of Epoxy Resin with Carbon-Fiber and Glass Surfaces. *Bull. Chem. Soc. Jpn.* **2017**, *90*, 500–505.
24. Henry, D. J.; Yiapanis, G.; Evans, E.; Yarovsky, I. Adhesion between Graphite and Modified Polyester Surfaces: A Theoretical Study. *J. Phys. Chem. B* **2005**, *109*, 17224–17231.
25. Köppen, S.; Bronkalla, O.; Langel, W. Adsorption Configurations and Energies of Amino Acids on Anatase and Rutile Surfaces. *J. Phys. Chem. C* **2008**, *112*, 13600–13606.
26. Köppen, S.; Langel, W. Simulation of Adhesion Forces and Energies of Peptides on Titanium Dioxide Surfaces. *Langmuir* **2010**, *26*, 15248–15256.
27. Mian, S. A.; Saha, L. C.; Jang, J.; Wang, L.; Gao, X.; Nagase, S. Density Functional Theory Study of Catechol Adhesion on Silica Surfaces. *J. Phys. Chem. C* **2010**, *114*, 20793–20800.

28. Mian, S. A.; Yang, L.-M.; Saha, L. C.; Ahmed, E.; Ajmal, M.; Ganz, E. A Fundamental Understanding of Catechol and Water Adsorption on a Hydrophilic Silica Surface: Exploring the Underwater Adhesion Mechanism of Mussels on an Atomic Scale. *Langmuir* **2014**, *30*, 6906–6914.
29. Bahlakeh, G.; Ghaffari, M.; Saeb, M. R.; Ramezanzadeh, B.; De Proft, F.; Terryn, H. A Close-up of the Effect of Iron Oxide Type on the Interfacial Interaction between Epoxy and Carbon Steel: Combined Molecular Dynamics Simulations and Quantum Mechanics. *J. Phys. Chem. C* **2016**, *120*, 11014–11026.
30. Ogata, S.; Takahashi, Y. Moisture-Induced Reduction of Adhesion Strength between Surface Oxidized Al and Epoxy Resin: Dynamics Simulation with Electronic Structure Calculation. *J. Phys. Chem. C* **2016**, *120*, 13630–13637.
31. Bikerman, J. J. *The Science of Adhesive Joints*, Academic Press, London, 1968.
32. Israelachvili, J. N. *Intermolecular and Surface Forces*, Revised 3rd ed.; Academic Press, London, **2011**.
33. Waite, J. H. Nature’s underwater adhesive specialist. *Int. J. Adhes. Adhes.*, **1987**, *7*, 9–14.
34. Crisp, D. J.; Walker, G.; Young, G. A.; Yule, A. B. Adhesion and Substrate Choice in Mussels and Barnacles. *J. Colloid Interface Sci.*, **1985**, *104*, 40–50.
35. Maier, G. P.; Rapp, M. V.; Waite, J. H.; Israelachvili, J. N.; Butler, A. Biological Adhesives. Adaptive Synergy between Catechol and Lysine Promotes Wet Adhesion by Surface Salt Displacement. *Science* **2015**, *349*, 628–632.
36. Wei, W.; Petrone, L.; Tan, Y.; Cai, H.; Israelachvili, J. N.; Miserez, A.; Waite, J. H. An Underwater Surface-Drying Peptide Inspired by a Mussel Adhesive Protein. *Adv. Funct. Mater.* **2016**, *26*, 3496–3507.
37. Iglesias, J. G.; González-Benito, J.; Aznar, A. J.; Bravo, J.; Baselga, J. Effect of Glass Fiber Surface Treatments on Mechanical Strength of Epoxy Based Composite Materials. *J. Colloid Interface Sci.* **2002**, *250*, 251–260.
38. Sekulic, A.; Curnier, A. An Original Epoxy-Stamp on Glass-Disc Specimen Exhibiting Stable Debonding for Identifying Adhesive Properties between Glass and Epoxy. *Int. J. Adhes. Adhes.* **2007**, *27*, 611–620.
39. Sekulic, A.; Curnier, A. Experimentation on Adhesion of Epoxy. *Int. J. Adhes. Adhes.*

2010, *30*, 89–104.

40. Ceresoli, D.; Bernasconi, M.; Iarlori, S.; Parrinello, M.; Tosatti, E. Two-Membered Silicon Rings on the Dehydroxylated Surface of Silica. *Phys. Rev. Lett.* **2000**, *84*, 3887–3890.
41. Iarlori, S.; Ceresoli, D.; Bernasconi, M.; Donadio, D.; Parrinello, M. Dehydroxylation and Silanization of the Surfaces of β-Cristobalite Silica: An *ab initio* Simulation. *J. Phys. Chem. B* **2001**, *105*, 8007–8013.
42. Yang, J.; Meng, S.; Xu, L. F.; Wang, E. G. Ice Tessellation on a Hydroxylated Silica Surface. *Phys. Rev. Lett.* **2004**, *92*, 146102.
43. Klier, K.; Shen, J. H.; Zettlemoyer, A. C. Water on Silica and Silicate Surfaces. I. Partially Hydrophobic Silicas. *J. Phys. Chem.* **1973**, *77*, 1458–1465.
44. Hair, M. L. Hydroxyl Groups on Silica Surface. *J. Non-Cryst. Solids* **1975**, *19*, 299–309.
45. Zhuravlev, L. T. Concentration of Hydroxyl Groups on the Surface of Amorphous Silicas. *Langmuir* **1987**, *3*, 316–318.
46. Nawrocki, J. The Silanol Group and Its Role in Liquid Chromatography. *J. Chromatogr. A* **1997**, *779*, 29–71.
47. D'Souza, A. S.; Pantano, C. G. Determination of the Surface Silanol Concentration of Amorphous Silica Surfaces Using Static Secondary Ion Mass Spectroscopy. *J. Vac. Sci. Technol.* **1997**, *A15*, 526–531.
48. D'Souza, A. S.; Pantano, C. G. Mechanisms for Silanol Formation on Amorphous Silica Fracture Surfaces. *J. Am. Ceram. Soc.* **1999**, *82*, 1289–1293.
49. Collins, K. E.; de Camargo, V. R.; Dimiras, A. B.; Menezes, D. T. C.; da Silva, P. A.; Collins, C. H. Physisorbed Water Layer Formation on Fully Hydroxylated Mesoporous Silicas. *J. Colloid Interface Sci.* **2005**, *291*, 353−360.
50. Tam, L.-h.; Lau, D. Moisture Effect on the Mechanical and Interfacial Properties of Epoxy-Bonded Material System: An Atomistic and Experimental Investigation. *Polymer* **2015**, *57*, 132–142.
51. *Materials Studio 6.1*, Accelrys Inc., San Diego, CA, 2012.
52. Perdew, J. P.; Burke, K.; Ernzerhof, M. Generalized Gradient Approximation Made Simple. *Phys. Rev. Lett.* **1996**, *77*, 3865–3868.

53. Grimme, S. Semiempirical GGA-Type Density Functional Constructed with a Long-Range Dispersion Correction. *J. Comput. Chem.* **2006**, *27*,1787–1799.

54. Gráfová, L.; Pitoňák, M.; Řezáč, J.; Hobza, P. Comparative study of selected wave function and density functional methods for noncovalent interaction energy calculations using the extended S22 data set. *J. Chem. Theory Comput.* **2010**, *6*, 2365– 2376.

55. Tkatchenko, A.; Scheffler, M. Accurate Molecular Van Der Waals Interactions from Ground-State Electron Density and Free-Atom Reference Data. *Phys. Rev. Lett.* **2009**, *102*, 073005.

56. Rigby, D.; Sun, H.; Eichinger, B. E. Computer Simulations of Poly(ethylene oxide): Force Field, PVD Diagram and Cyclization Behavior. *Polym. Int.* **1997**, *44*, 311– 330.

57. Sun, H. COMPASS: An ab initio Force-Field Optimized for Condensed-Phase Applications-Overview with Details on Alkane and Benzene Compounds. *J. Phys. Chem. B* **1998**, 102, 7338–7364.

58. Sun, H.; Ren, P.; Fried, J. The COMPASS Force Field Parameterization and Validation for Phosphazenes. *Comput. Theor. Polym. Sci.* **1998**, *8*, 229–246.

59. Patel, S. K.; Lavasanifar, A.; Choi, P. Roles of Nonpolar and Polar Intermolecular Interactions in the Improvement of the Drug Loading Capacity of PEO-b-PCL with Increasing PCL Content for Two Hydrophobic Cucurbitacin Drugs. *Biomacromolecules* **2009**, *10*, 2584– 2591.

60. Kang, G.J.; Chen, Z.X.; Li, Z.; He, X. A theoretical study of the charge state and size of gold clusters on the adsorption and dissociation of H_2. *J. Chem. Phys.* **2009**, *130*, 034701.

Chapter 3. Pair Interaction Energy Decomposition Analysis (PIEDA) at the Adhesive Interface between Epoxy Resin Layer and Silica Surface

3-1. Introduction

Adhesion technology is widely used in various industries, such as construction, automotive, aerospace, sports equipment, and electronics, due to its lightness, mechanical strength, and insulation properties.[1] Adhesion technology has been advancing day by day, and a lot of experimental-based research has been conducted for various applications.[2,3,4] However, the principles underlying it are not fully understood due to its complexity. In other words, the theory of adhesion is still in its infancy, leaving the possibility for new research.

One of the most common adhesives, epoxy resins can be readily employed in many manufacturing processes, including pultrusion, molding, and coating.[5] Of the various epoxy resins, the bisphenol A-type epoxy resin shown in Figure 3-1a, which is produced via the polymerization of diglycidyl ether of bisphenol A (DGEBA) shown in Figure 3-1b, is used in this study. The epoxy resin contains OH and -O- groups that can form H-bonds with an hydrophilic adherend. One common application of epoxy resins is the polymer matrix of fiber-reinforced plastic (FRP), which is a composite material made of synthetic polymers and fibers.[6] FRP is used commercially in the aerospace industry, the automotive industry, civil engineering and construction, and sporting goods. In these applications, the mechanical properties of the product are altered by the interfacial interaction between the adhesive and the adherend. In this study, an epoxy resin/silica interface modeled on the structure of glass fiber reinforced plastic (GFRP) is theoretically investigated.

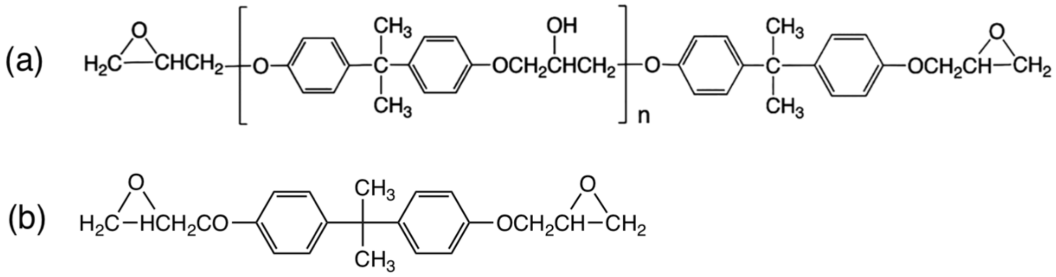

Figure 3-1. Structural formulae of (a) bisphenol A-type epoxy resin (polymer) and (b) its monomer, DGEBA.

As shown in Figure 3-2, the silica surface is known to be terminated with silanol groups, which are assumed to be generated by the reaction with water in air.[7] From this, it can be inferred that H-bonds are formed between the OH and -O- groups of the epoxy resin (Figure 3-1a) and the silanol groups on the silica surface. Previous studies have revealed H-bonding interactions between the epoxy resin and the silica surface based on the optimized structure, and the H-bonding interactions were found to play an important role in improving the adhesive bond strength.[8,9]

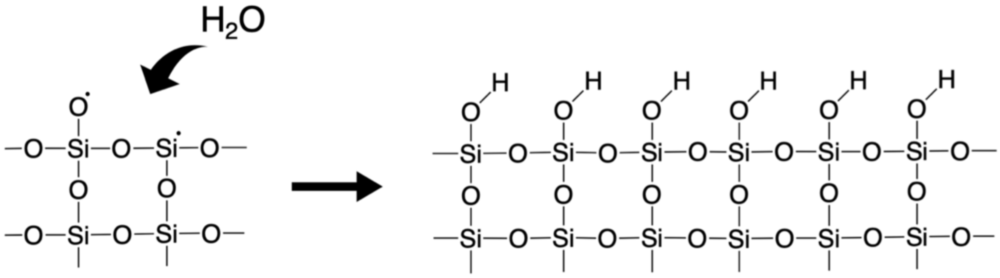

Figure 3-2. Schematic representation of the chemisorption process of water molecules on a bare silica surface. Dots denote surface dangling bonds.

In addition to the structural features, the interaction energy (ΔE_{int}) is useful for evaluating interfacial interactions. Pair interaction energy decomposition analysis (PIEDA) is a quantum chemical method for decomposing ΔE_{int} between N-body fragments into electrostatic contributions (ΔE_{es}), exchange repulsion (ΔE_{ex}), charge transfer (ΔE_{ct}), and dispersion (ΔE_{disp}) as follows:[10,11]

$$\Delta E_{\text{int}} = \Delta E_{\text{es}} + \Delta E_{\text{ex}} + \Delta E_{\text{ct}} + \Delta E_{\text{disp}}. \qquad (3\text{-}1)$$

The interfacial interaction between the epoxy resin and silica surface has been clarified by using the PIEDA, leading us to the conclusion that the synergistic effects of the electrostatic and dispersion interactions are important in the OH-functionalized surfaces of the armchair edge of graphite and alpha-cristobalite.[8] Thus, decomposing ΔE_{int} may provide useful insight into the mechanisms of adhesive interactions that cannot be understood via structural features alone. However, the epoxy resin was modeled with a part of the repeating unit of the bisphenol A-type epoxy resin in the previous study.[8]

The behavior of polymer chains in the thickness direction of polymer layers is of great interest in the field of polymer science. Polymer chains exhibit different structures depending on the layer to which they belong. For example, it was found that adsorption polymer layer of poly(vinyl alcohol) (PVA) on a Si substrate consists of two or three layers under humid conditions; one is inner adsorption layer strongly constrained on the substrate, another is loosely adsorbed outer layer due to the large distance from the inner layer, and the other is middle layer between them which appeared with a high degree of saponification of PVA.[12] Thus, effects of polymer layers on interfacial adhesive interaction cannot be ignored when one try to understand the adhesive phenomena, and the epoxy resin is not exception of this.

The present study is designed to confirm that the synergistic effects of ΔE_{es} and ΔE_{disp} can be maintained in the interface model with an epoxy resin layer on the hydrophilic silica surface by using the PIEDA. The epoxy layer model is composed of 20 monomers of the DGEBA without polymerization, to reduce the computational costs and to reach a more understandable analysis inside of the epoxy layer. Both the behavior of the entire epoxy layer and the behavior of each epoxy molecule consisting the epoxy layer are investigated to elucidate the interfacial adhesive interaction between epoxy resin and silica surface at the molecular level.

3-2. Methods

3-2-1. Modeling of the periodic epoxy layer

The monomer structure of DGEBA shown in Figure 3-1b was used as a component of the epoxy layer model. Considering the polymerization and curing process, the epoxide rings were opened at both ends of DGEBA as shown in Figure 3-3a, and the structure shown in Figure 3-3b was used as a component of the epoxy layer. Hereafter, the ring-opened DGEBA monomer will be referred to as “epoxy molecule”.

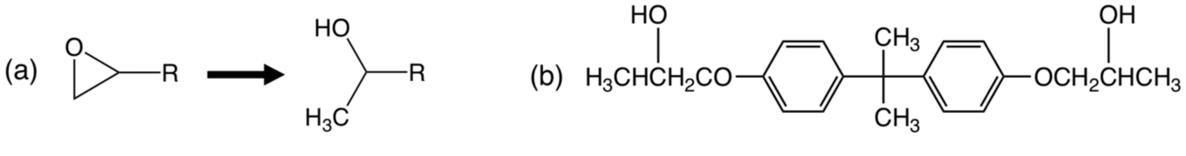

Figure 3-3. (a) Ring opening of edge epoxide groups of DGEBA and (b) the epoxy molecule used in this study as the component of the epoxy layer.

The epoxy layer was constructed by filling a periodic cubic cell with 20 epoxy molecules as shown in Figure 3-4. The Amorphous Cell module implemented in Materials

Studio 2016[13] was used to construct the epoxy layer. Three initial layer models were constructed according to the self-avoiding random walk method proposed by Theodorou and Suter.[14] The output cubic structure was disordered and homogeneous, and periodic boundary conditions were applied to the x and y axes. The lattice constants were set to a = 30 Å and b = 30 Å. The density of the epoxy resin layer was set to 1.13 g/cm^3[15] and thereby lattice constant c was automatically fixed to 11 Å. The most energetically stable structure of the initial three structures was selected as a representative epoxy layer.

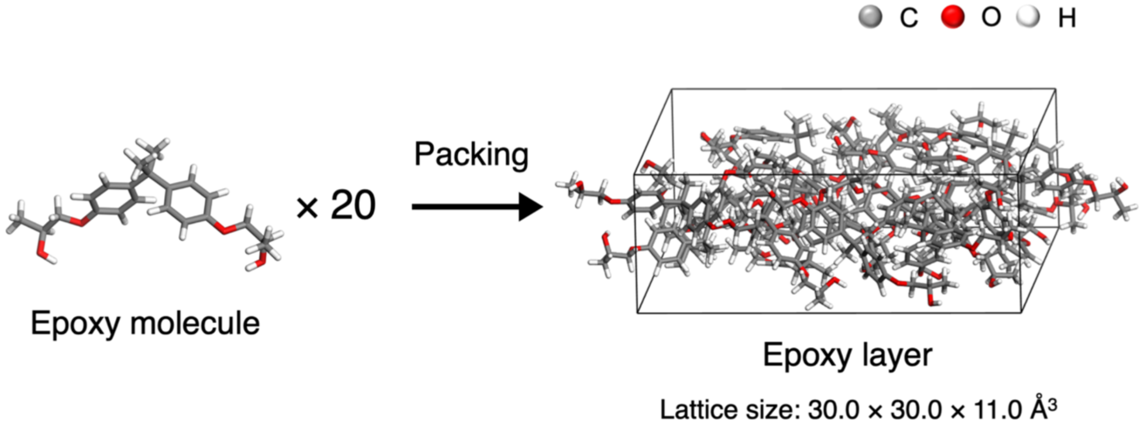

Figure 3-4. The construction of the periodic epoxy layer consists of 20 epoxy molecules. The lattice constants were set to a = 30 Å and b = 30 Å, while that of c was automatically fixed based on the density value of 1.13 g/cm^3.[15]

3-2-2. Modeling of the periodic silica surface

The periodic silica surface was built from the bulk structure of α-cristobalite as shown in Figure 3-5. The bulk structure was fully optimized beforehand using DFT calculations, and a slab model of the unit cell was created by cleaving α-cristobalite at the (0 0 1) surface and adding a 40 Å vacuum layer. The unit cell contains 6 Si atoms and 12 O atoms with lattice parameters of a = 5 Å, b = 5 Å, c = 50 Å. Two water molecules were dissociatively adsorbed on the upper and lower layers of the cleaved surface, resulting in hydroxylated silica surfaces. The surface contains two OH groups attached to each Si atom. The density of OH groups on the surface is 8 OH per nm^2. This is close to the typical density of 5 OH per nm^2, which is measured for an amorphous silica experimentally.[16] The structure of the hydroxylated silica surface was fully optimized by using DFT calculations with the Vienna Ab initio Simulation Package (VASP) software [17], [18], [19], [20] The generalized gradient approximation of Perdew−Burke−Ernzerhof (GGA-PBE) [21], [22] was adopted for the exchange−correlation functional with D2 dispersion correction by Grimme.[23] A plane-wave basis set cutoff of 500 eV, self-consistent field tolerance of 1.0×10^{-5} eV, Brillouin zone sampling on a grid spacing of $2\pi \times 0.05$ Å^{-1}, and 0.05 eV/Å threshold of forces on atoms guaranteed good convergence. Ultimately, the unit cell was expanded to the 6 × 6 supercell with lattice parameters of a = 30 Å, b = 30 Å, and c = 50 Å.

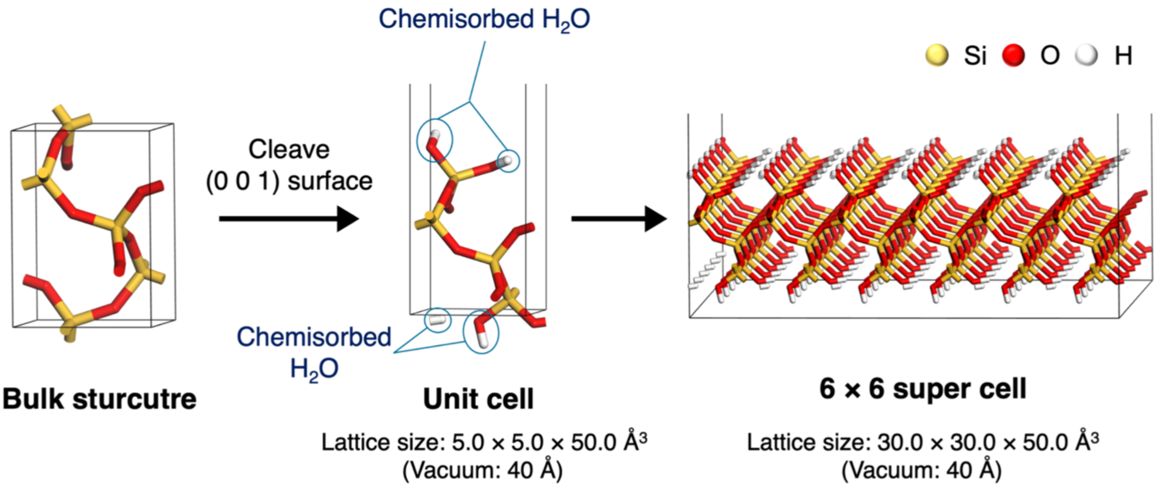

Figure 3-5. The process of constructing silica surface model and the dimensions of the model built. The upper and lower silica surfaces were hydroxylated by H_2O from bulk structure of α-cristobalite. The bulk structure of α-cristobalite was obtained from the database implemented in Material Studio 2016.[13]

3-2-3. Construction of the periodic interfacial model of the epoxy layer and silica interface

The slab model of adhesion interface was built by integrating the representative epoxy layer and the 6 × 6 supercell of silica surface. The epoxy layer was placed on the silica surface as shown in Figure 3-6a using the Build Layers dialog implemented in Materials Studio 2016.[13] The periodic lattice parameters are a = 30 Å, b = 30 Å, c = 54 Å, including a 30 Å vacuum layer. The periodic model of the adhesive interface contains 1708 atoms per lattice.

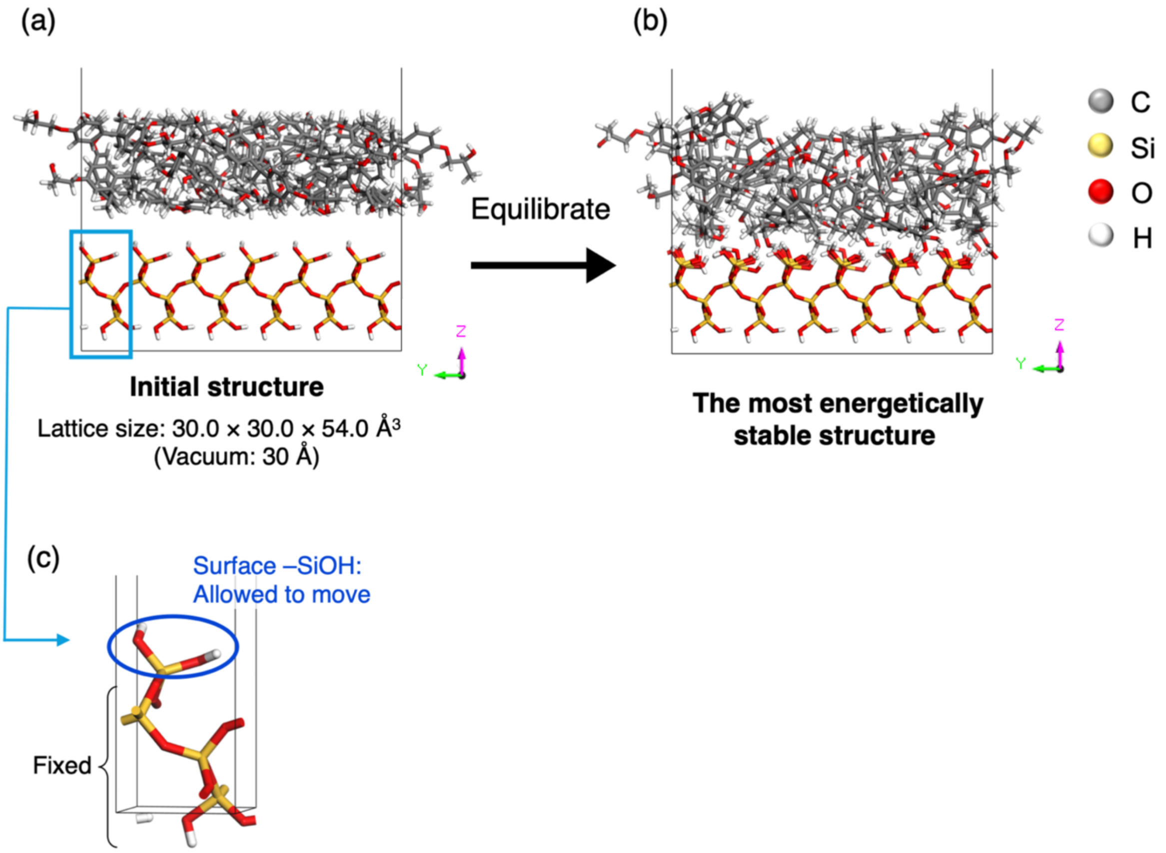

Figure 3-6. Adhesion interface equilibration. (a) Initial structure of the adhesive interface constructed by combining the epoxy layer and the silica surface and (b) the most energetically stable structure selected among 1,000 optimized structures after quench dynamics. (c) Surface –SiOH groups were allowed to move during the quench dynamics.

Quench dynamics simulation, which is a feature of the Forcite program implemented in Materials Studio 2016,[13] was performed to equilibrate the adhesive interface. This module combines geometry optimization and molecular dynamics (MD) to explore the conformational space for low-energy structures by sampling at fixed points along a classical MD trajectory. We sampled the structure for every 1 ps frame of a 1 ns MD simulation and optimized the structures with molecular mechanics (MM) geometry optimization. The system was maintained at a constant temperature (300 K) using an NVT ensemble with a Nosé-Hoover thermostat.[24,25,26] The total dynamics time was set to 1 ns with a time step of 1 fs. The COMPASS force field[27,28,29] was chosen to describe the inter- and intra-molecular interactions to effectively predict the properties of polymer materials.[30] The van der Waals interactions and Coulomb potentials were calculated through the atom-based and Ewald approach. For the MM geometry optimization, the energy and force convergence thresholds were set to be 0.001 kcal/mol and 0.5 kcal mol^{-1} Å^{-1}, respectively. Eventually, the most energetically stable structure of 1,000 optimized structures was chosen as a representative epoxy adhesive/silica interface (Figure 3-6b). This periodic model is hereafter referred to as "Layer model". During the quench dynamics, the upper silanol groups (–SiOH) were allowed to move, while the other atoms of the silica surface were kept fixed, as shown in Figure 3-6c.

3-2-4. PIEDA calculations of the Layer model

PIEDA calculations were applied to 20 epoxy molecules in the Layer model individually, and the calculated energies were summed up to estimate total ΔE_{int}, ΔE_{es}, ΔE_{ex}, ΔE_{ct}, and ΔE_{disp} of the Layer model as shown in Figure 3-7. Each of 20 epoxy molecules was cut out from the periodic Layer model with a clustered silica surface, which was tailored to each epoxy molecule. The structures of epoxy molecules and silica surfaces in the 20 clustered models were kept as they were in the Layer model, and edge dangling bonds of clustered silica surfaces were terminated with H atoms. Effects of many-body interactions and sizes of the clustered silica surfaces on the ΔE_{int} appeared to be insignificant from a preliminary investigation, which enabled us to calculate interaction energies of the 20 epoxy molecules separately.

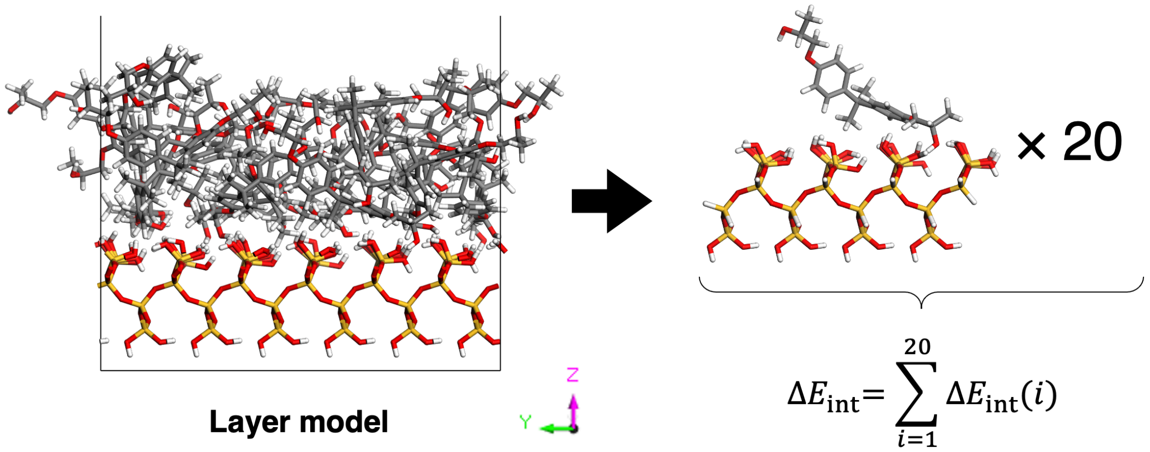

$$\Delta E_{\mathrm{int}} = \sum_{i=1}^{20} \Delta E_{\mathrm{int}}(i)$$

Figure 3-7. Construction of 20 cluster models from the Layer model for PIEDA. The 20 different clusters consisting of an epoxy molecule and a silica surface cluster were constructed, and total values of ΔE_{int}, ΔE_{es}, ΔE_{ex}, ΔE_{ct}, and ΔE_{disp} of the Layer model were calculated by summing up each calculated energy of the 20 epoxy molecules.

Interaction energies were calculated by using the *ab initio* fragment molecular orbital method[31] at the HF/6-31G(d) level of theory. To estimate ΔE_{disp}, calculated Hartree-Fock (HF) energies were corrected for dispersion interactions by using Grimme's dispersion correction scheme D2.[23] On the basis of the geometries of the 20 epoxy/silica clustered models, PIEDA implemented in the GAMESS program package[32] was carried out to determine the energetic components governing the adhesive interactions.

3-3. Results and discussion

3-3-1. ΔE_{int} and its decomposed energies of the Layer model

Table 3-1 shows calculated energies of the 20 clustered models built from the Layer model. The calculated energies include ΔE_{int}, ΔE_{es}, ΔE_{ex}, ΔE_{ct}, ΔE_{disp}, ratios of the decomposed energies to $\Delta E_{\mathrm{int},}$ and total energies. The clustered models were sorted by the ratio of ΔE_{disp} from the smallest to the largest and assigned in the order of a to t. The unit of mJ/m^2, which is usually used for the work of adhesion (W_{ad}) in the experimental field, was used in this study. The surface area of 900 Å^2 (30 Å × 30 Å) of silica, which is the unit cell size of the periodic model, was used to convert the raw data in kcal/mol to mJ/m^2. As seen in Table 3-1, total energies of ΔE_{int}, ΔE_{es}, ΔE_{ex}, ΔE_{ct}, and ΔE_{disp} of the Layer model are 365.4 mJ/m^2, 407.9 mJ/m^2, –400.1 mJ/m^2, 135.8 mJ/m^2, and 221.8 mJ/m^2, respectively. Ratios to ΔE_{int} of the four decomposed energies calculated from these total energies are as follows: ΔE_{es} shows the highest ratio of 1.12; ΔE_{ex} shows the ratio of –1.10, whose absolute value was less than ΔE_{es} but almost as large as it; ΔE_{ct} shows the ratio of 0.37, which is the smallest contribution to ΔE_{int}; ΔE_{disp} shows the ratio of 0.61, which is not ignorable as a part of adhesive interaction. This is substantially the same results as those of our previous model,[8] which demonstrates that the synergistic effects of ΔE_{es} and ΔE_{disp} on the adhesive interaction are also essential at the interface of the Layer model with the epoxy layer.

Table 3-1. The ΔE_{int}, decomposed energies, their ratios to ΔE_{int}, and total energies calculated from the 20 clustered models.

Models	Energies (mJ/m^2)					Ratios to ΔE_{int}			
	ΔE_{int}	ΔE_{es}	ΔE_{ex}	ΔE_{ct}	ΔE_{disp}	ΔE_{es}	ΔE_{ex}	ΔE_{ct}	ΔE_{disp}
a	0.1	0.1	0.0	0.0	0.0	1.00	0.00	0.00	0.00
b	–0.1	–0.1	0.0	0.0	0.0	1.00	0.00	0.00	0.00
c	7.3	5.2	–0.7	1.1	1.6	0.72	–0.10	0.15	0.23
d	13.9	17.4	–14.0	4.3	6.2	1.25	–1.01	0.31	0.45
e	24.5	33.9	–30.9	9.3	12.2	1.38	–1.26	0.38	0.50
f	24.8	29.9	–26.8	9.1	12.6	1.20	–1.08	0.37	0.51
g	32.2	33.7	–28.9	10.1	17.4	1.05	–0.90	0.31	0.54
h	42.9	47.1	–43.4	15.2	24.1	1.10	–1.01	0.35	0.56
i	29.5	28.7	–26.0	9.9	16.9	0.97	–0.88	0.34	0.57
j	33.4	37.2	–36.5	12.6	20.1	1.11	–1.09	0.38	0.60
k	33.8	44.0	–46.9	14.8	21.9	1.30	–1.39	0.44	0.65
l	29.6	29.9	–32.6	11.5	20.8	1.01	–1.10	0.39	0.70
m	29.5	31.2	–33.6	11.2	20.7	1.06	–1.14	0.38	0.70
n	19.1	18.7	–20.3	7.2	13.5	0.98	–1.07	0.38	0.71
o	28.8	32.7	–37.1	12.6	20.6	1.13	–1.29	0.44	0.71
p	4.9	1.3	–0.8	0.7	3.7	0.26	–0.17	0.15	0.76
q	8.7	17.6	–21.5	5.9	6.7	2.02	–2.47	0.68	0.77
r	1.2	0.2	0.0	0.0	1.0	0.15	0.00	0.02	0.83
s	0.8	–0.3	0.0	0.1	1.0	–0.40	–0.02	0.18	1.23
t	0.4	–0.2	0.0	0.0	0.7	–0.53	0.00	0.01	1.51
Total	365.4	407.9	–400.1	135.8	221.8	1.12	–1.10	0.37	0.61

3-3-2. The interaction area making up more than 99% of ΔE_{int}

Among the 20 clustered models, there are some epoxy molecules that do not directly contribute to the interfacial interaction. As shown in Table 3-1, models a, b, r, s, and t shows less than 1.2 mJ/m^2 of ΔE_{int}, which indicates that they have almost no interaction with the silica surface. In other words, epoxy molecules in models from c to q make a large contribution to the interfacial interaction with the silica surface. In fact, total ΔE_{int} of them is 363.0 mJ/m^2, which is 99.3 % of the total ΔE_{int} of the whole Layer model. Figure 3-8 shows structures of the 20 clustered models assigned from a to t that correspond to the models in Table 3-1. The dot line in Figure 3-8 is the border line located 3.6 Å from the silica surface. This border divides the area occupied by the 5 non-interacting molecules from the area occupied by the 15 interacting molecules. Therefore, interfacial interaction between the epoxy layer and the silica surface occurs in the area of 3.6 Å from the silica surface, accounting for more than 99% of total ΔE_{int} of the Layer model.

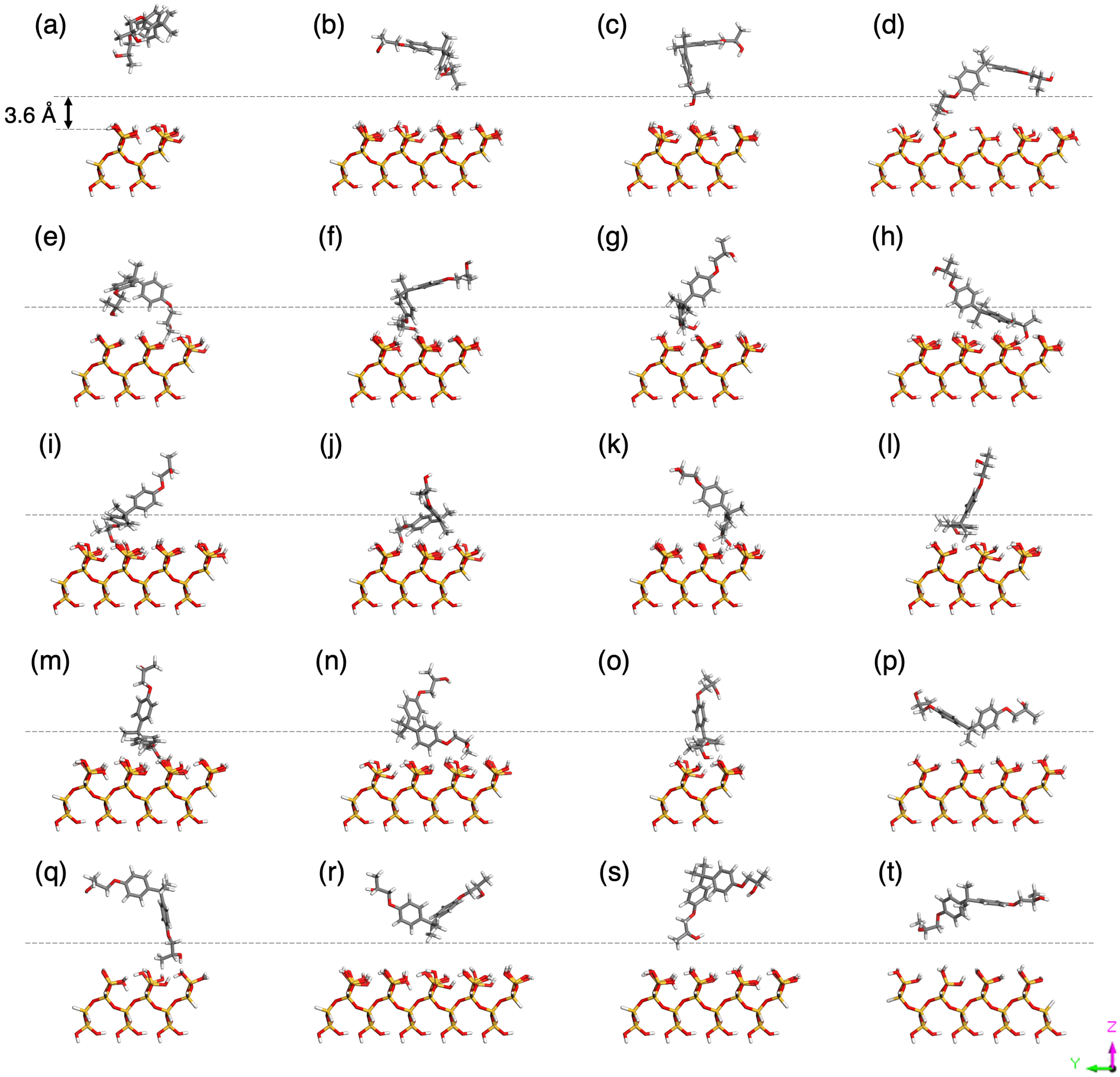

Figure 3-8. Structures of 20 calculation models consists of an epoxy molecules and a clustered silica surface cut out from the Layer model. Gray, yellow, red, and white sticks represent C, Si, O, and H atoms, respectively. The black dot line is the border line located 3.6 Å from the silica

surface, which divide the area occupied by the 5 non-interacting molecules from the area occupied by the 15 interacting molecules.

The region of 3.6 Å would be far from the thickness of experimentally measured inner adsorption layer. The inner adsorption layer of PVA on a Si substrate mentioned in the introduction is in nm order of 2.3–3.2 nm, which varies depending on saponification degrees and humidity conditions.[12] This inconsistency between computation and experiment is normal because the actual polymer has a chain composed of hundreds or thousands of repeating units (1700 in the study of PVA[12]). They are intricately intertwined each other and constrain themselves onto the substrate even when the edges of the polymer chains a few nm away from the surface. Under different conditions between computation and experiment, however, our results suggest that the 3.6 Å area is the origin of the inner adsorption layer that has the strongest interfacial interaction between the epoxy layer and silica surface.

3-3-3. Comparison between ΔE_{int} and W_{ad} with their decomposed energies

Theoreticians are not the only ones who enjoy the benefits of energy decomposition. Experimental people working in the field of polymer chemistry have conducted an energy decomposition for W_{ad}. Strictly speaking, decomposed energies are demanded to estimate surface free energies (γ) of solid surfaces, eventually to estimate W_{ad} of solid–solid interfaces experimentally. Eq (3-2) is the way to estimate W_{ad} of solid–solid interfaces derived by combining Dupré equation[3,33] and extended Fowkes (Kitazaki and Hata) equation.[34,35]

$$W_{\mathrm{ad}} = 2\sqrt{\gamma_1^{\mathrm{p}}\gamma_2^{\mathrm{p}}} + 2\sqrt{\gamma_1^{\mathrm{d}}\gamma_2^{\mathrm{d}}} + 2\sqrt{\gamma_1^{\mathrm{h}}\gamma_2^{\mathrm{h}}} = W_{\mathrm{ad}}^{\mathrm{p}} + W_{\mathrm{ad}}^{\mathrm{d}} + W_{\mathrm{ad}}^{\mathrm{h}}, \tag{3-2}$$

where γ_i^{p}, γ_i^{d}, and γ_i^{h} are γ of the solid phase i decomposed into polarization, dispersion, and H-bonding components. $W_{\mathrm{ad}}^{\mathrm{p}}$, $W_{\mathrm{ad}}^{\mathrm{d}}$, and $W_{\mathrm{ad}}^{\mathrm{h}}$ represents polarization, dispersion, and H-bonding components of W_{ad}, corresponding to each term in the middle of eq (3-2). They were newly defined in this study in order to express eq (3-2) as an energy decomposition definition of W_{ad}, not only as a equation for estimating W_{ad}.

The energy decomposition of W_{ad}, especially the ratio of $W_{\mathrm{ad}}^{\mathrm{d}}$, can help us to verify our PIEDA results. Kinloch and co-workers estimated W_{ad} of epoxy adhesive/silica interface to be

178 mJ/m^2 from eq (3-2), where γ^p and γ^d of the epoxy adhesive were 5.0 mJ/m^2 and 41.2 mJ/m^2; γ^p and γ^d of the silica were 209 mJ/m^2 and 78mJ/m^2, respectively.[36,37] In that study, γ^h of the extended Fowkes equation was excluded. Therefore, as shown in Table 3-2, W_{ad}^p and W_{ad}^d of the epoxy adhesive/silica interface can be estimated to be 65 mJ/m^2 and 113 mJ/m^2, and their ratios to W_{ad} are 0.36 and 0.64, respectively. Results in Table 3-1 and Table 3-2 indicate that ΔE_{int} tend to overestimate W_{ad}, while ratios of ΔE_{disp} and W_{ad}^d are consistent. W_{ad}^p supposed to include the other ΔE_{int} components of ΔE_{es}, ΔE_{ex}, and ΔE_{ct}. However it is still unclear how to decompose W_{ad}^p into the three components for the comparison between them, which will not be covered in this study.

Table 3-2. W_{ad} and its components of the epoxy adhesive/silica interface. The ratios of W_{ad}^p and W_{ad}^d to W_{ad} were also calculated.

Energies (mJ/m^2)			Ratios to W_{ad}	
W_{ad}	W_{ad}^p	W_{ad}^d	W_{ad}^p	W_{ad}^d
178	65	113	0.36	0.64

The overestimation of W_{ad} by ΔE_{int} and the consistency between ratios of ΔE_{disp} and W_{ad}^d can be explained by the difference of definition between them. Computational adhesive energies and forces have tended to exceed experimental values in our previous works.[9,38] We have discussed these overestimations were due to the absence of some factors in computational models that supposed to exist in the real system, such as interfacial water, air atmosphere, curing agents, and impurities contamination. However, it is more important in this study that ΔE_{int} and W_{ad} are fundamentally different approaches, not just differences between computation and experiment. W_{ad} is defined as the work required to separate the unit area of two phases in contact.[3] This includes the energy change by structural relaxation after adhesive failure, while ΔE_{int} does not take the structural relaxation into account. Therefore, the overestimation of W_{ad} by ΔE_{int} is convincing. On the other hand, if we assume the structural relaxation affects W_{ad}^p and W_{ad}^d equally, ratios of ΔE_{int} and W_{ad} are comparable because the difference of structural relaxation between them can be ignored. We suppose this is the reason why ratios of ΔE_{disp} is consistent with W_{ad}^d. Thus, ratios of dispersion components are reasonable to compare ΔE_{int} and W_{ad} rather than their energy values.

3-3-4. Detailed analyses of the 15 epoxy molecules in the 3.6 Å interacting area

Based on the ratio of $W_{\mathrm{ad}}^{\mathrm{d}}$ (0.64), we have proceeded to structural analyses of the 15 epoxy molecules in the 3.6 Å interacting area. The ratio of ΔE_{disp} showed comparable result with the ratio of $W_{\mathrm{ad}}^{\mathrm{d}}$; however, as shown in Table 3-1, the 15 models from c to q have wide range of ΔE_{disp} ratio from 0.23 to 0.77. As explained already, Table 3-1 is sorted by ratios of ΔE_{disp} from the smallest to the largest. Therefore, ΔE_{disp} ratios of models from c to j are below the ratio of $W_{\mathrm{ad}}^{\mathrm{d}}$, while ΔE_{disp} of models from k to q are above it. The average of these ΔE_{disp} results in the ΔE_{disp} ratio of the entire Layer model, which is close to the ratio of $W_{\mathrm{ad}}^{\mathrm{d}}$. However, there are no similarities or structural patterns that can distinguish their ratios of ΔE_{disp} higher or lower than $W_{\mathrm{ad}}^{\mathrm{d}}$ ratio. As seen in Figure 3-8, there are rather structural similarities between models that have different (high and low) ΔE_{disp} ratios. In other words, there are various reasons why each epoxy molecule shows a ratio higher or lower than $W_{\mathrm{ad}}^{\mathrm{d}}$ ratio, and it becomes clear by comparing similar structures within the 15 models.

The simplest model pair, which has structural similarity but with ΔE_{disp} difference, is models c and p. As shown in Figure 3-9, the OH group of model c and the CH_3 group of model p are located within the 3.6 Å border. Therefore, model c shows large ΔE_{es} and model p shows large ΔE_{disp}, resulting in ΔE_{disp} ratio of c to be low (0.23) and ΔE_{disp} ratio of p to be high (0.76) as shown in Table 3-1. This model pair is easy to explain the origin of their ratios of ΔE_{disp}. However, there are complicated models that are difficult to find the structural differences to explain the ΔE_{disp} ratio differences, and PIEDA results give us feedback to find them. As a matter of fact, ΔE_{disp} ratios depend on the magnitude relation between ΔE_{es} and ΔE_{ex}; as seen in Table 3-1, ΔE_{disp} ratios are lower than $W_{\mathrm{ad}}^{\mathrm{d}}$ ratio when $\Delta E_{\mathrm{es}} > |\Delta E_{\mathrm{ex}}|$, while ΔE_{disp} ratios are higher than $W_{\mathrm{ad}}^{\mathrm{d}}$ ratio when $\Delta E_{\mathrm{es}} < |\Delta E_{\mathrm{ex}}|$. Therefore, ΔE_{disp} ratios are mainly controlled by ΔE_{es} and ΔE_{ex} indirectly, except the case of model p affected by ΔE_{disp} magnitude directly.

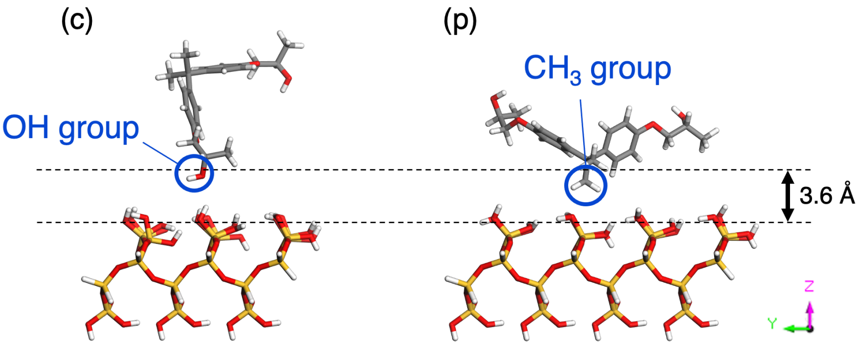

Figure 3-9. Comparison of models c and p. The area between the dashed lines with a distance of 3.6 Å represents the interaction area.

3-3-5. ΔE_{es}, ΔE_{ex}, and H-bonding interaction

ΔE_{ex} identifies the difference of ΔE_{disp} ratio between models d and q, regardless of their structural similarity. Models d and q have the ends of epoxy molecules interacting with the silica surface and forming a single H-bond each, as shown in Figure 3-10. However, their ΔE_{disp} ratios are 0.45 for d (lower than W_{ad}^{d} ratio) and 0.77 for q (higher than W_{ad}^{d} ratio). Observing energy differences of ΔE_{es}, ΔE_{ex}, ΔE_{ct}, and ΔE_{disp} helps to clarify the reason for this. Looking at their energy differences in Table 3-1, ΔE_{ex} of q is 7.7 mJ/m^2 more negative than ΔE_{ex} of d, which is the largest difference among the four components. This ΔE_{ex} difference should be because of the distance between the epoxy molecule and the silica surface. Indeed the H-bonding distances of d and q are 1.71 Å and 1.62 Å as shown in Figure 3-10. Since ΔE_{ex} is repulsive energy, the short distance between epoxy molecule and silica surface makes ΔE_{ex} large in negative. The end CH_3 group of q is also closer to the silica surface than that of d according to the z-coordinates of each C atom in the CH_3 group. They are 11.78 Å for d and 11.31 Å for q as shown in Figure 3-10. On the other hand, ΔE_{disp} values were almost the same between d and q, regardless of the distance difference between the epoxy molecule and the silica surface. This is actually consistent with the sensitivity of ΔE_{ex} and ΔE_{disp} to the distance of epoxy resin from the silica surface; the energy–distance curve for ΔE_{ex} decreases rapidly as the epoxy resin is displaced farther from the silica surface, whereas the value of ΔE_{disp} decreases at a relatively slow rate.[8] Therefore, ΔE_{ex} controls ΔE_{disp} ratios of d and q indirectly.

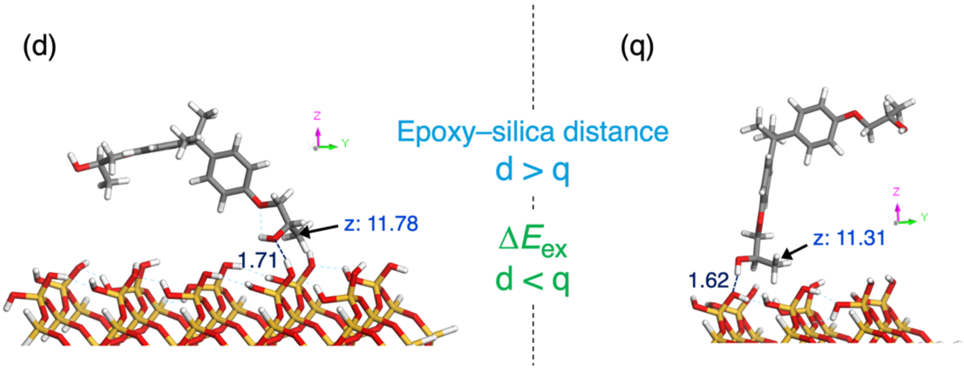

Figure 3-10. Comparison of models d and q. The dashed blue lines represent the H-bonds formed between the epoxy molecule and the silica surface that are responsible for the interfacial interaction, and the distances are shown in Å. The z-coordinates of the C atoms indicated by the black arrows are shown after “z:” in Å.

The ΔE_{disp} ratios of models e, f, and n vary due to the difference in ΔE_{es}. The epoxy molecules e, f, and n shown in Figure 3-11 are similar in that the epoxy ends mainly interact with the silica surface and their structures are overall closer to the silica surface than the above d and q, leading ΔE_{int} of e (24.5 mJ/m^2), f (24.8 mJ/m^2), and n (19.1 mJ/m^2) about 10 mJ/m^2 larger than ΔE_{int} of d (13.9 mJ/m^2) and q (8.7 mJ/m^2). However, their ratios of ΔE_{disp} are different among them; e shows 0.50 and f shows 0.51 (lower than $W_{\mathrm{ad}}{}^{\mathrm{d}}$ ratio), while n shows 0.71 (higher than $W_{\mathrm{ad}}{}^{\mathrm{d}}$ ratio). Comparing energy differences of ΔE_{es}, ΔE_{ex}, ΔE_{ct}, and ΔE_{disp}, the largest difference is ΔE_{es} for both cases between e and n, and between f and n. ΔE_{es} is mainly derived from H-bonding interactions, and structures in Figure 3-11 shows different number of H-bonds between them. There are two H-bonds in e and three in f. In the case of n, only one H-bond is formed. Thus, the ΔE_{disp} ratios of models e, f, and n varies due to the difference in ΔE_{es}, which comes from the number of H-bonds.

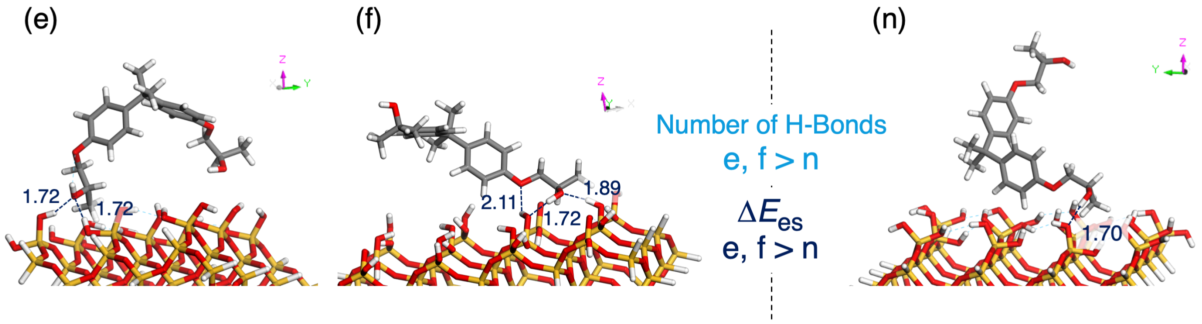

Figure 3-11. Comparison of models e, f, and n. The blue dashed lines indicate the H-bonds formed between the epoxy molecule and the silica surface, which are responsible for the interfacial interaction, and the distance between them is shown in Å.

3-3-6. The balance of OH/π interaction, H-bonding interaction, and ΔE_{es}

The models shown so far have had only epoxy end interactions with the silica surface, however, OH/π interactions are strongly involved in the 5 models of h, j, l, m, and o. OH/π interactions of these 5 models are shown in Figure 3-12a, where the presence of OH/π interaction was determined from their structures. H-bonds between their end OH groups or -O- groups and the silica surface are also observed as shown in Figure 3-12b. Despite these commonalities, ΔE_{disp} ratios of h and j are 0.56 and 0.60 (higher than W_{ad}^{d} ratio), while ΔE_{disp} ratios of l, m, and o are 0.70, 0.70, and 0.71 (lower than W_{ad}^{d} ratio), respectively. The largest energy difference between them is ΔE_{es} of the four energy components, originating from either OH/π interaction or H-bonding interaction, and it controls ΔE_{disp} ratios of these 5 models.

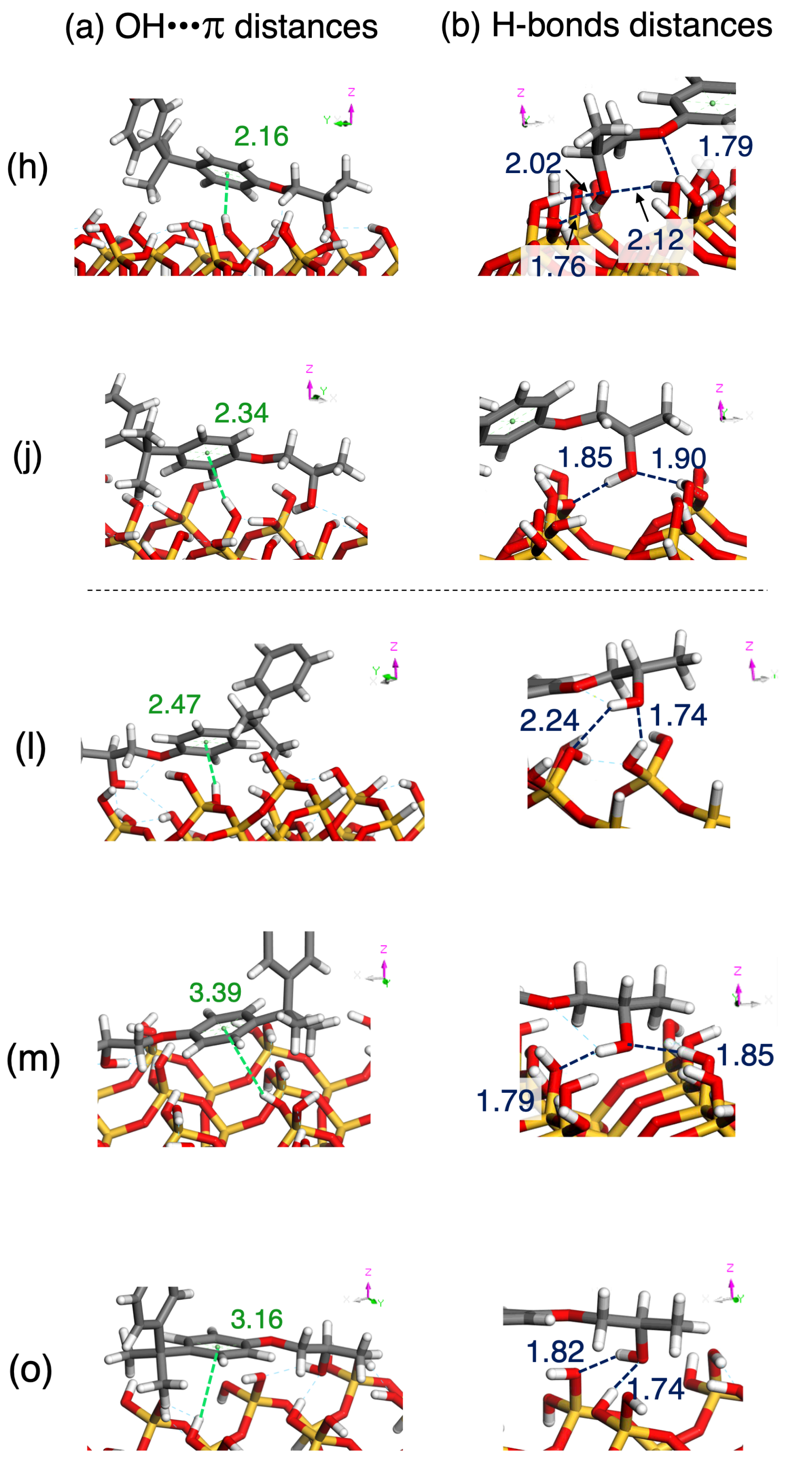

Figure 3-12. Comparison of models h and j with l, m, and o. OH/π interactions are shown in (a), and H-bonds between the epoxy molecule and the silica surface are shown in (b). All distances are in Å.

First of all, model h is unique compared to the other four models. As shown in Table 3-1, ΔE_{es} of h (47.1 mJ/m^2) is much larger than ΔE_{es} of j (37.2 mJ/m^2), l (29.9 mJ/m^2), m (31.2 mJ/m^2), and o (32.7 mJ/m^2). This is because h forms an overwhelmingly number of H-bonds between the epoxy molecule and the silica surface, as shown in Figure 3-12b. The other ΔE_{int} components of h are also larger (though ΔE_{ex} is compared on the negative energy scale) than those of j, l, m, and o, indicating that the distance between the epoxy molecule and the silica surface is very short in h. Therefore, model h is unique because all of the components are larger than those of j, l, m, and o, and ΔE_{es} is especially large in the four components, which lead the model h to the lower ΔE_{disp} ratio than $W_{\mathrm{ad}}{}^{\mathrm{d}}$ ratio.

The ΔE_{es} difference between model j and models m and o can be explained by OH/π interaction. As shown in Figure 3-12a, the OH•••π distances of j (2.34 Å) is much shorter than that of m (3.39 Å) and o (3.16 Å), which results in that the OH/π interaction of m and o is less significant than the OH/π interaction of j. On the other hand, the H-bonds of m (1.79 Å, 1.85 Å) and o (1.74 Å, 1.82 Å) are slightly stronger than those of j (1.85 Å, 1.90 Å). Thus, the large difference of ΔE_{es} between j and m or j and o are caused by OH/π interaction, leading model j to show lower ΔE_{disp} than $W_{\mathrm{ad}}{}^{\mathrm{d}}$, and also leading models m and o to show higher ΔE_{disp} than $W_{\mathrm{ad}}{}^{\mathrm{d}}$.

In the case of models j and l, on the contrary, the strength of the H-bonding interaction is the key to distinguish their ΔE_{es} difference. As shown in Figure 3-12a, the OH•••π distances in j and l are 2.34 Å and 2.47 Å, respectively. The OH/π interaction in j should be slightly greater than that that of l. On the other hand, the strength of the H-bonding interaction cannot be measured from its length; both j and l form two H-bonds between the OH groups and the silica surface. Basically, the shorter length of the H-bond should result in a stronger interaction. However, one of the H-bonds in j (1.90 Å) is shorter than that in l (2.24 Å), and the other H-bond in j (1.85 Å) is longer than that in l (1.74 Å). It is difficult to say which H-bonding interaction is stronger than other ones. As a solution, it is useful to compare the overall structures of j and l. As shown in Figure 3-13, the OH group of l is farther away from the silica surface than that of j based on their z-coordinates. Therefore, the H-boning interactions of j should be stronger than those of l. Thus, the strength of the H-bonding interactions makes a difference in ΔE_{es} between j and l. Since the H-bonding interaction is stronger than the OH/π interaction, the difference in ΔE_{es} between j and l, resulting from the H-bonding interaction, is greater than the difference between j and m, or between j and o, resulting from the OH/π interaction.

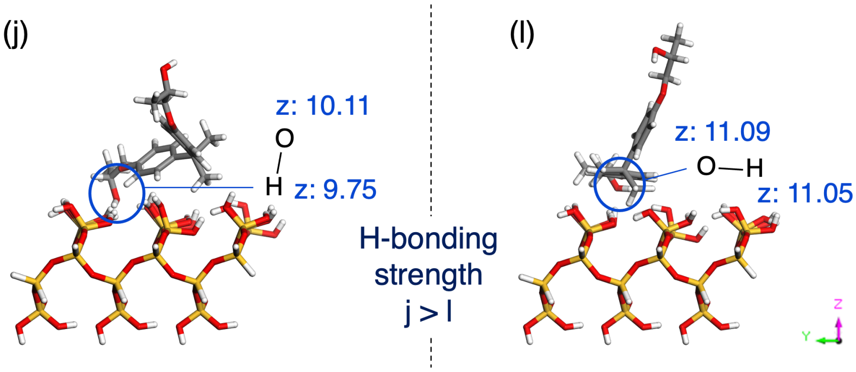

Figure 3-13. Comparison of H-bonding strength between models j and l. The positions of the OH groups clearly indicate a difference between j and l. The z-coordinates of end O and H atoms are shown after "z:" in Å.

3-3-7. Effects of ΔE_{ex} on the remaining three structures

Models g, i, and k, the remaining models of the 15 interacting models, are similar to the 5 molecules in the previous section in that one of the benzene rings is close to the silica surface in addition to the OH group at the end. However, they have no OH/π interaction. Regardless of the commonalities of models g, i, and k, ΔE_{disp} ratios of models g and i are 0.54 and 0.57 (lower than W_{ad}^{d} ratio), while that of model k is 0.65 (higher than W_{ad}^{d} ratio). In this case, ΔE_{ex}, originated from the position of end OH groups, controls their ΔE_{disp} ratios. Figure 3-14 shows z-coordinates of the end OH groups of epoxy molecules g, i, and k. Since the OH group of k is closer to the silica surface than the OH groups of g and i, ΔE_{es} of k (44.0 mJ/m^2) is larger than ΔE_{es} of g (33.7 mJ/m^2) and i (28.7 mJ/m^2). However, more importantly, ΔE_{ex} of k is negatively greater than ΔE_{ex} of g and i due to the proximity of the epoxy molecule to the silica surface. This is the reason why the ΔE_{disp} ratios of g and i are lower W_{ad}^{d} ratio, and ΔE_{disp} ratio of k is higher than W_{ad}^{d} ratio.

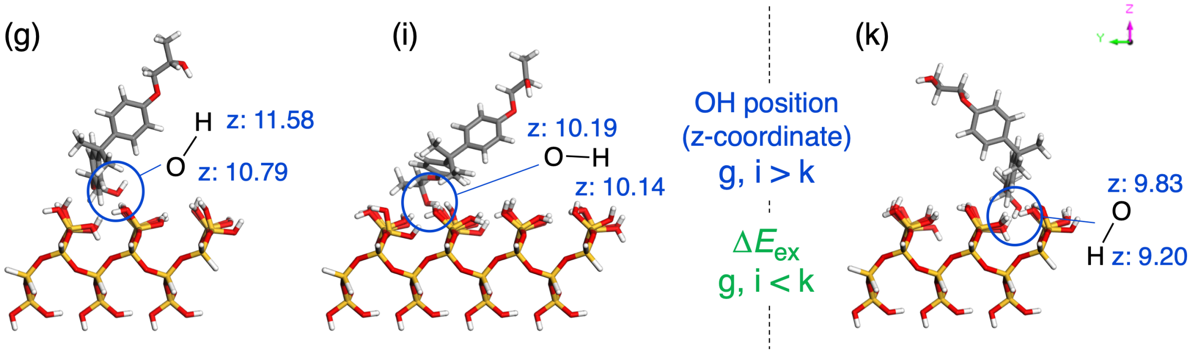

Figure 3-14. The z-coordinates of the end OH groups of the epoxy molecules g, i, and k. The z-coordinates of the O and H atoms are shown after “z:” in Å.

3-4. Conclusions

The adhesive interface composed of an epoxy layer and a silica surface was investigated to analyze the effect of epoxy layer on the adhesive interaction. Periodic interfacial model, named Layer model in this study, was prepared by using DFT calculations and quench dynamics, and PIEDA was applied to the 20 epoxy–silica clusters modeled from the periodic Layer model. As a result, distributions of ΔE_{es}, ΔE_{ex}, ΔE_{ct}, and ΔE_{disp} in ΔE_{int} of the Layer model demonstrates that the synergetic effects of ΔE_{es} and ΔE_{disp} on the adhesive interaction are essential at the epoxy resin/silica interface. The investigation of the 20 cluster models also revealed that more than 99% of ΔE_{int} of the Layer model comes from the area within 3.6 Å from the silica surface, where 15 of the 20 epoxy molecules are involved.

The ΔE_{disp} ratio of the Layer model has a good agreement with the ratio of $W_{\mathrm{ad}}{}^{\mathrm{d}}$, which shows the consistency between computation and experiment. Based on the ratio of $W_{\mathrm{ad}}{}^{\mathrm{d}}$, we have proceeded the detailed analyses of the 15 epoxy molecules in the 3.6 Å interaction area. Most of the ΔE_{disp} ratios of 15 models, except model p, are controlled by ΔE_{es} and ΔE_{ex}. These energies are significantly related to either H-bonding interaction or OH/π interaction, or both. PIEDA gives us a correct answer to determine the critical structural features that control ΔE_{int} and its components. The results described in this paper have provided new insights into the evaluation of adhesive interaction energies with detailed structural features at the molecular level. Further studies with decomposed $W_{\mathrm{ad}}{}^{\mathrm{p}}$ should shed further light on these phenomena and may lead to a deeper understanding of the interfacial adhesive properties.

References

1. Ebnesajjad, S; Landrock, A. H. *Adhesives technology handbook,* 3rd ed.; William Andrew: London, 2015; pp 1–18.
2. *Fundamentals of adhesion*; Lee, L. H. Ed.; Springer Science+Business Media: New York, 1991.
3. *Handbook of Adhesion Technology*; da Silva, L. F. M., Öchsner, A., Adams, R. D. Eds.; Springer Science+Business Media: Berlin, Germany, 2011.
4. *Handbook of Adhesive Technology*; Pizzi, A., Mittal, K. L., Eds.; Marcel Dekker, Inc.: New York, 2003.
5. Petrie, E. M. Epoxy adhesives. In *Epoxy Adhesive Formulations*; McGraw-Hill Education:New York, 2005; Ch. 1, pp 1–26.
6. Petrie, E. M. Composites. In *Epoxy Adhesive Formulations*; McGraw-Hill Education:New York, 2005; Ch. 16.4, pp 378–381.
7. Klier, K.; Shen, J. H.; Zettlemoyer, A. C. Water on Silica and Silicate Surfaces. I. Partially Hydrophobic Silicas. *J. Phys. Chem.* **1973**, *77* (11), 1458–1465.
8. Yoshizawa, K.; Semoto, T.; Hitaoka, S.; Higuchi, C.; Shiota, Y.; Tanaka, H. Synergy of Electrostatic and van Der Waals Interactions in the Adhesion of Epoxy Resin with Carbon-Fiber and Glass Surfaces. *Bull. Chem. Soc. Jpn.* **2017**, *90* (5), 500–505.
9. Higuchi, C.; Tanaka, H.; Yoshizawa, K. Molecular Understanding of the Adhesive Interactions between Silica Surface and Epoxy Resin: Effects of Interfacial Water. *J. Comput. Chem.* **2019**, *40* (1), 164–171.
10. Kitaura, K.; Morokuma, K. A new energy decomposition scheme for molecular interactions within the Hartree-Fock approximation. *Int. J. Quantum Chem.* **1976**, *10*, 325–340.
11. Fedorov, D. G.; Kitaura, K. Pair Interaction Energy Decomposition Analysis. *J. Comput. Chem.* **2006**, *28*, 222–237.
12. Miyazaki, T.; Miyata, N.; Yoshida, T.; Arima, H.; Tsumura, Y.; Torikai, N.; Aoki, H.; Yamamoto, K.; Kanaya, T.; Kawaguchi, D.; Tanaka, K. Detailed Structural Study on the Poly(Vinyl Alcohol) Adsorption Layers on a Si Substrate with Solvent Vapor-Induced Swelling. *Langmuir* **2020**, *36* (13), 3415–3424.
13. Dassault Systèmes BIOVIA, Materials Studio 2016, San Diego, CA, 2005.

14. Theodorou, D. N.; Suter, U. W. Detailed Molecular Structure of a Vinyl Polymer Glass. *Macromolecules* **1985**, *18* (7), 1467–1478.

15. Rider, A. N.; Brack, N.; Andres, S.; Pigram, P. J. The Influence of Hydroxyl Group Concentration on Epoxy-Aluminium Bond Durability. *J. Adhes. Sci. Technol.* **2004**, *18*, 1123−1152.

16. Zhuravlev, L. T. Concentration of Hydroxyl Groups on the Surface of Amorphous Silicas. *Langmuir* **1987**, *3* (3), 316–318.

17. Kresse, G.; Hafner, J. Ab Initio Molecular Dynamics for Liquid Metals. *Phys. Rev. B* **1993**, *47* (1), 558–561.

18. Kresse, G.; Hafner, J. Ab Initio Molecular-Dynamics Simulation of the Liquid-Metalamorphous- Semiconductor Transition in Germanium. *Phys. Rev. B* **1994**, *49* (20), 14251–14269.

19. Kresse, G.; Furthmüller, J. Efficiency of Ab-Initio Total Energy Calculations for Metals and Semiconductors Using a Plane-Wave Basis Set. *Comput. Mater. Sci.* **1996**, *6*, 15–50.

20. Kresse, G.; Furthmüller, J. Efficient Iterative Schemes for Ab Initio Total-Energy Calculations Using a Plane-Wave Basis Set. *Phys. Rev. B* **1996**, *54* (16), 11169–11186.

21. Perdew, J. P.; Burke, K.; Ernzerhof, M. Generalized Gradient Approximation Made Simple. *Phys. Rev. Lett.* **1996**, *77* (18), 3865–3868.

22. Perdew, J. P.; Burke, K.; Ernzerhof, M. Generalized Gradient Approximation Made Simple (Vol 77, Pg 3865, 1996). *Phys. Rev. Lett.* **1997**, *78* (1992), 1396–1396.

23. Grimme, S. Semiempirical GGA-type density functional constructed with a long-range dispersion correction. *J. Comput. Chem.* **2006**, *27*, 1787–1799.

24. Nosé, S. A Molecular Dynamics Method for Simulations in the Canonical Ensemble. *Mol. Phys.* **1984**, *52* (2), 255–268.

25. Nosé, S. A Unified Formulation of the Constant Temperature Molecular Dynamics Methods. *J. Chem. Phys.* **1984**, *81* (1), 511–519.

26. Hoover, W. G. Canonical Dynamics: Equilibrium Phase-Space Distributions. *Phys. Rev. A* **1985**, *31* (3), 1695–1697.

27. Rigby, D.; Sun, H.; Eichinger, B. E. Computer Simulations of Poly(ethylene oxide): Force Field, PVD Diagram and Cyclization Behavior. *Polym. Int.* **1997**, *44*, 311– 330.

28. Sun, H. COMPASS: An ab initio Force-Field Optimized for Condensed-Phase Applications-Overview with Details on Alkane and Benzene Compounds. *J. Phys. Chem. B* **1998**, 102, 7338–7364.

29. Sun, H.; Ren, P.; Fried, J. The COMPASS Force Field Parameterization and Validation for Phosphazenes. *Comput. Theor. Polym. Sci.* **1998**, *8*, 229–246.

30. Gao, L.; Zhang, Q.; Li, H.; Yu, S.; Zhong, W.; Sui, G.; Yang, X. Effect of Epoxy Monomer Structure on the Curing Process and Thermo-Mechanical Characteristics of Tri-Functional Epoxy/Amine Systems: A Methodology Combining Atomistic Molecular Simulation with Experimental Analyses. *Polym. Chem.* **2017**, *8* (13), 2016–2027.

31. Gordon, M. S.; Fedorov, D. G.; Pruitt, S. R.; Slipchenko, L. V. Fragmentation Methods: A Route to Accurate Calculations on Large Systems. *Chem. Rev.* **2012**, *112* (1), 632–672.

32. Schmidt, M. W.; Baldridge, K. K.; Boatz, J. A.; Elbert, S. T.; Gordon, M. S.; Jensen, J. H.; Koseki, S.; Matsunaga, N.; Nguyen, K. A.; Su, S.; Windus, T. L.; Dupuis, M.; Montgomery, J. A. General Atomic and Molecular Electronic Structure System. *J. Comput. Chem.* **1993**, *14* (11), 1347–1363.

33. Schrader, M. E. Young-Dupre Revisited. *Langmuir* **1995**, *11* (9), 3585–3589.

34. Kitazaki, Y.; Hata, T. Surface-Chemical Criteria for Optimum Adhesion. *J. Adhes.* **1972**, *4* (2), 123–132.

35. Fowkes, F. M. ATTRACTIVE FORCES AT INTERFACES. *Ind. Eng. Chem.* **1964**, *56* (12), 40–52.

36. Kinloch, A. J. Interfacial Fracture Mechanical Aspects of Adhesive Bonded Joints—a Review. *J. Adhes.* **1979**, *10* (3), 193–219.

37. Kinloch, A. J; Dukes, W. A; Gledhill, R. A. *Adhesion Science and Technology, Part B*; Lee, L-H Ed.; Plenum Press: New York,1975; pp 597–614.

38. Semoto, T.; Tsuji, Y.; Yoshizawa, K. Molecular Understanding of the Adhesive Force between a Metal Oxide Surface and an Epoxy Resin: Effects of Surface Water. *Bull. Chem. Soc. Jpn.* **2012**, *85* (6), 672–678.

Chapter 4. Prediction of the Glass Transition Temperatures of Linear Homo/heteropolymers and Cross-linked Epoxy Resins

4-1. Introduction

Glass transition temperature (T_g) is the temperature at which the polymer transfers from a rigid glass state to a soft rubber state. At this temperature there is sufficient free volume to allow molecules in the polymer backbone to move, so that rigid backbone relaxes and causes a transition from a solid polymer material to a quasi-liquid state.[1–3] Below the T_g, molecules can oscillate and vibrate around a fixed position creating a certain amount of free volume, which is dependent upon the temperature of the system. T_g plays an important role in determining the processing and performance properties such heat resistance, durability, and adhesion of the polymer since heat capacity, coefficient of thermal expansion, and viscosity are affected by glass transition. T_g is generally measured using Differential Scanning Calorimetry (DSC) or Dynamic Mechanical Thermal Analysis (DMTA).[1–2,4] Glass transition occurs over a relatively wide temperature range and depends on conditions such as measurement method, experimental period, and pressure under measurement.[1,5] T_g is also highly dependent on the structure of the polymer (crosslinking, chain stiffness), constitutive (additives, fillers, impurities), and conformation (stereo regularity). Therefore, it is difficult to uniquely determine by experiment, and the differences between the reported values of T_g in literature can be very large.

Numerous T_g prediction models have been already developed.[2–3, 6–21] Krevelen and co-workers developed the basis of group additive property (GAP) method.[6–7] The GAP method predicts polymer T_gs as a sum of calibrated contributions associated to typical substructures present in the monomers. Starting from here, many studies have been attempted to improve prediction accuracy and applicability domain by calibrating the contributions for additional substructures. Bicerano used a data set of 320 polymers[2] to build a model that combined a weighted sum of structural parameters along with the solubility parameter of each polymer. A linear regression procedure was used to produce a model with a standard deviation of 24.65 K and a correlation coefficient of 0.9749. However, no external data set compounds were withheld to validate this model. Most of these approaches gave relatively good predictive correlations, but they are only applicable for polymers containing chemical structural groups previously investigated.

At the end of the 1980's, more general QSPR (Quantitative Structure–Property

Relationships)-based T_g predictions were developed.[11–14] Hopfinger and co-workers used molecular modeling to generate polymer descriptors (conformational entropy, mass moments, and intermolecular interactions) used to complement the group-specific terms in GAP models.[11–12] Waegell and co-workers approached modeling by using an Energy, Volume, Mass (EVM) QSPR model.[13–14] For linear and branched aliphatic acrylate and methacrylate polymers, the standard deviation from linear regression was 12 K with an R^2 value of 0.96. This model allowed the prediction of polymer T_g values not used for training of the original multiple linear regression, with an average absolute error of 10%. In the 1990's, T_g prediction focused on models without explicit knowledge of polymer 3D structure and without falling back to a predefined set of substructures of known contributions.[3,15–18] Katritzky and co-workers generated over 400 constitutional, topological, geometrical, and quantum chemical descriptors directly from the molecular structure of the unit block in the polymer with the Comprehensive Descriptors for Structural and Statistical Analysis (CODESSA) program.[15–16] They showed that T_g divided by the molar weight of the repeating unit (M) improved squared correlation coefficient, resulting in an R^2 value of 0.946. In cross-validation of their training set, the T_g values for the 88 linear homopolymers, from the results of T_g/M prediction, with a standard error of 0.33 K mol g^{-1}.

All the discussed approaches for predicting T_g values were developed on the basis of homopolymers, despite the importance of epoxy-amine copolymers in commercial applications. There are, however, studies concerning a small number on amine-cured epoxy resins.[19–21] Bellenger et al. predicted about 40 T_gs of epoxy-amine copolymers based on the additivity law for copolymers and the contribution of cross-linked structures.[20] They have compared several physical and empirical approaches of the effect of cross-linking on T_g. Morrill et al. have predicted T_gs for epoxy-amine copolymers with the CODESSA program.[21] They succeeded to predict the T_g changes depending on the epoxy-amine molar ratio. However, their data set was rather limited.

So far, thus, most T_g prediction studies use molecular descriptors of the repeat unit in the polymer, which implies that they are only applicable to homopolymers $–(A)_n–$ or linear 1:1 heteropolymers $–(AB)_n–$ which can formally be regarded as "homopolymers" of unit AB. By contrast, repeating units cannot be always found in epoxy resins forming a network structure. As a result, T_g prediction of linear homopolymer and epoxy–amine copolymers were so far treated separately, because of assumed incompatibility of input descriptors: classical molecular descriptors of the repeat unit, on one hand, *versus* a combination of descriptors of copolymer reagents (and information about molar ratios) for epoxy-amine resins.

Since epoxy–amine copolymers form a complicated 3D network structure, we herein advocate focusing on copolymer reagent structures (the polyamines and polyepoxides) and their molar fraction to generate "implicit" descriptors for the resulting polymer. In Silico design and Data Analysis (ISIDA) descriptors[22–23] monitor the occurrence of user-defined fragments in compounds, furthermore supporting "marked-atom"[24] strategies (where specified atoms are "marked" in the input structure and herewith acquire special status: the molecular fragments containing marked atoms will hence be counted separately from fragments occurring in the non-marked molecular "bulk"). This approach is perfectly suited to capture structural information about the copolymer reagents, all while marking the atoms involved in the formation of new bonds during the polymerization process. Marked-atom descriptors of the copolymerization reagents can then be combined (with optionally weighing by their molar ratio) into a final descriptor vector of the copolymer. This approach is however not limited to epoxy-amine copolymers, but also applies for linear 1:1 heteropolymers $–(AB)_n–$ of other chemical classes, thus opening the perspective of a more general T_g prediction model. For example, polyamides will be described by the combined descriptors of the dicarboxylic acid with marked carboxyl carbon and diamine with marked amino N atoms. Eventually, the present study undertook one more step towards generalization: it was assumed that homopolymers $–(A)_n–$ can be formally described as *1:1 copolymers of A with itself, and herewith amenable to the same description protocol as implemented for genuine copolymers.* This original strategy enabled the first-time development of a unified, homo- and heteropolymer-competent T_g prediction model. Implicitly, the now possible fusion of the various local datasets exploited in previous studies lead to an unprecedented wealth of training information and external validation opportunities. Support Vector Regression (SVR)[25] was used for modeling, driving the selection of best-suited polymer description schemes (which result from the several considered marked-atom monomer fragmentation schemes and monomer descriptor combination strategies). Generative Topographic Mapping (GTM)[26–28] was employed to create a 2D map of "polymer chemical space", highlighting the various classes of (co)polymers included in the study, and being used to analyze the features and problems of the predictive model. Proceeding in three steps, T_g models of increasing generality are realized: (1) T_g prediction is performed on Katritzky's data set of homo- and linear $–(AB)_n–$ copolymers, for which published modeling results serve as a benchmark to assess the pertinence of the herein proposed method. Next, (2) an epoxy-resin-specific model was developed, based on T_g data set of epoxy resin gathered from published literatures. Finally, (3) a global data set including both linear and reticulated homo- and heteropolymer was compiled and used to fit the general, final model. Models obtained at steps (2) and (3) are publicly available on the QSAR prediction web server http://infochim.u-strasbg.fr/webserv/VSEngine.html.

4-2. Methods

4-2-1. Data Sources

To support the modeling workflow shown in Figure 4-1, T_g values of 389 polymers were collected from the literature. 270 of these constituted the “global” set for the general model. They contain

(i) 88 compounds of Katritzky’s set.[16] These also served to build an alternative model to the published one, with the herein proposed technology for benchmarking purposes (by cross-validation),

(ii) 50 epoxy resins,[21,29–40] which also served for calibration of an epoxy resin-specific model, and

(iii) 132 homo- and heteropolymers from Bicerano et al.,[2] which only contributed to the global set (no “local” model was fitted for these). These were selected because they included completely novel chemotypes shown to fall outside the Applicability Domain (AD) of the local model (i).

The remaining 119 polymers, composed of 102 linear and 17 epoxy-amine copolymers were kept apart, as test sets for external validation. The 17 epoxy resins represent the novel compounds listed in ref 20 but not already present amongst the 50 compounds mentioned above (ii). They served both in the test set of the global model as well as for the epoxy-resin-specific model (ii). The 102 linear homo/heteropolymers stem from Bicerano’s article and were kept as external test after exclusion of the 132 items which were mandatorily part of training set as chemically complementary to Katritzky’s polymers.

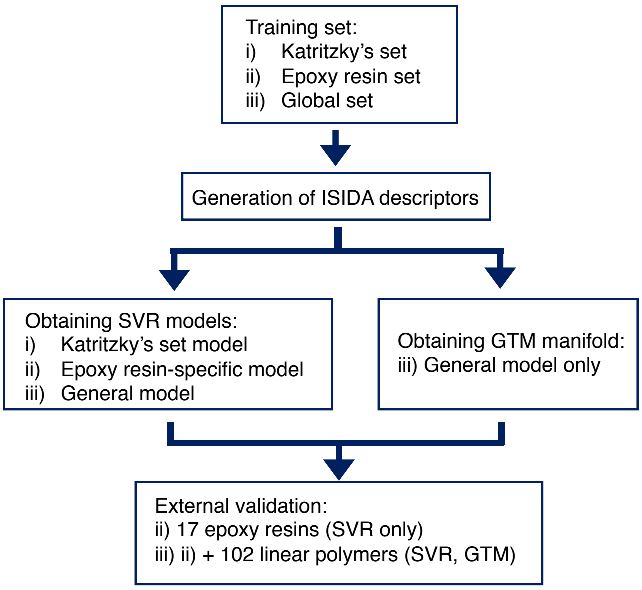

Figure 4-1. Workflow for the modeling of the T_g for homopolymers and copolymers.

4-2-2. Data preparation

The training data used in the present work was compiled from the various precursory articles mentioned above. However, given the herein targeted goal of a maximal generality model, structural data had to be significantly reorganized and standardized to fit our purposes. As already mentioned, the most general case is represented by heteropolymers – thus, the input required for modeling must contain the structures of the two monomers involved in copolymerization (dot-concatenated SMILES of the two species must be prepared for input). Implicitly, in homopolymers the structure of the only monomer "copolymerizing" with itself must also be reported twice. As the studied polymers result from diverse chemistries, there is no clear rule to define which of the two monomers must be reported first in the SMILES pair – therefore, the order in which the two SMILES are concatenated is irrelevant. However, another key request is to report (in the second column of SMILES file), the molar ratio of the first monomer in the SMILES pair. For example, in a reticulated epoxy-amine resin incorporating two moles of triamine A for three moles of diepoxy compound E, the input line can be either "E.A 0.6" or "A.E 0.4", where 0.6 is the molar fraction of E (3/5) and 0.4 is the one of A (2/5). For a homopolymer of monomer M, the input line will invariably be "M.M 0.5"

Before employment in model building, monomer structures must undergo structure standardization. Since the ultimate goal of this work was to achieve publicly available models operating on our multipurpose QSAR prediction server, submitted structures will necessarily undergo the thereon implemented "classical" standardization protocol (removal of counterions and mixtures – this specific option can and must be toggled off to allow processing of above-mentioned input files, e.g. standardize every mixture component –, conversion to “basic” aromatic form, split-charge nitro groups, etc.). For this reason, it is required to enter the “formal structures” of monomer reagents rather than structures of unit fragments in the polymer chain (with unsatisfied valences). These “formal structures” of the reagents are those atom-marked representations of the reagents which are easiest to convert to the polymeric form (with a minimal rearrangement of bonds). Polyethylene –$[CH_2\text{-}CH_2]_n$- can be obviously derived from the structure of it monomer, ethylene – which coincides with the “formal structure” [CH2:1]=[CH2:1] to be used (note “:1” represents the mapping labels associated to the atoms connecting to other monomers – the same map label “1” can be used for all atoms involved in polymerization). However, as shown in Figure 4-2, –$[CH_2\text{-}CH(OH)]_n$- is the polymerization product of acetaldehyde,

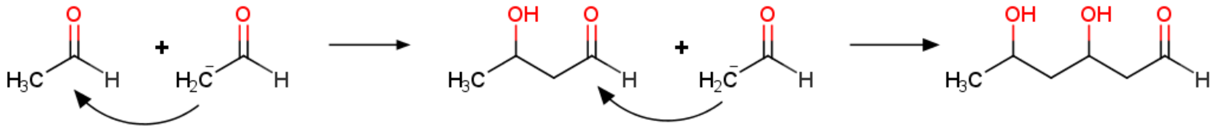

Figure 4-2. Polymerization of acetaldehyde.

a reaction proceeding by the addition of the carbanion resulting from α-proton extraction by a base to the carbonyl group. Formally it is nevertheless easier to describe this polymer as “polyvinylalcohol” stemming from [CH2:1]=[CH2:1]O. The key rule adopted in this work is to minimize the number of marked atoms, involved in bonds being formed or changing bond order. With vinyl alcohol, only the two carbons need to be marked. By contrast, taking acetaldehyde as such for monomer would require flagging of both carbons *and* the carbonyl O. Using this concept of “formal structures” for monomers, even copolymers in which the chain unit stems from three molecules may be described by a pair of formal structures. For example, above-mentioned polyvinylalcohols may react with another aldehyde, forming 1,3-dioxane rings as stable acetals. The product (Figure 4-3) may nevertheless be described in a way that is compatible with modeling constraints, by assuming the two “formal” copolymer structures to be (i) the vinyl alcohol and (ii) the vinylalcohol hemiacetal of the ring-closing aldehyde. Both all the “ethylene” carbons (as responsible for the C-C concatenation) as well as the vinyl alcohol O and the hemiacetal carbon C(O)(X)OH need to be marked. The latter couple is responsible for dioxane ring closure – with elimination of water, which corresponds to the unmarked -OH of the hemiacetal.

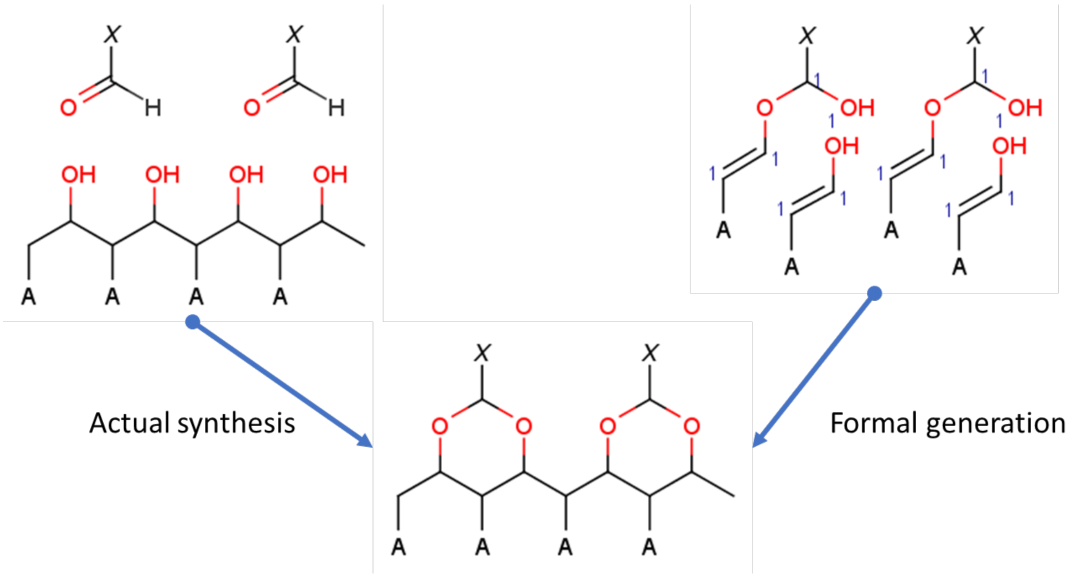

Figure 4-3. Actual synthesis and formal representation of a polymer containing a 1,3-dioxane-based unit resulting from ring closure by acetal formation in a reaction following the formation of the polyvinylalcohol chain. Formally, this can be described as the "copolymerization" of a vinyl alcohol molecule with the hemiacetal formed by another vinyl alcohol molecule and the ring-closing aldehyde.

As could be seen in the above-mentioned example, some polymerization processes (the archetypical ones being polyamide or polyester synthesis) involve elimination of some leaving groups (typically -OH, e.g. formation of water). This leaving group is kept in the reacting monomers, even though it will be absent in the actual polymer for which prediction of T_g is attempted. Owing to the fact that a leaving -OH group is by definition connected to a marked carbon participating in reaction, this signature can be allegedly exploited by the machine learning algorithm to differentially treat leaving -OH by contrast to regular hydroxy groups in the polymer. However, leaving groups other than -OH (it is chemically possible to obtain polyamides by reacting diamines with diacyl chlorides, with HCl as coproduct, for example) should be rendered as -OH in "formal" monomer structures, for coherence (not following this rule will place the input structure outside the model's applicability domain). Note that Bicerano's set also feature two "atypical" polytriazine imide-based structures: these were ignored in the present study. Albeit they could be formally represented according to a scheme similar to Figure 4-3, they were excluded from the study because they are radically new chemotypes, and two of them are clearly not enough to allow any meaningful learning of specific features of this polymer class.

4-2-3. ISIDA (In Silico design and Data Analysis) descriptors

To generate fragment descriptors, ISIDA Fragmentor 2017[41] was applied to each reacting monomer, as rendered after the standardization step. ISIDA descriptors are topological fragments descriptors based on 2D chemical structures.[22–24] The length of monitored fragments carried from 2 to 15 for sequences, from 1 to 5 for atom-centered fragments, and from 3 to 7 for triplets. The following options were also used at choice: charges on atoms (FormalCharge), accounting for the terminal atoms of a fragment exclusively (AtomPairs), exploring all possible paths instead of shortest paths (AllPaths) or restricted paths (Restricted). All employed fragmentation schemes generated both default fragments and specific fragments containing marked atoms (marked-atom strategy #3). Refer to the above-cited Fragmentor manual for technical details about these options. A total of 84 different fragmentation schemes were generated, in order to select the best suited one for modeling.

The actual polymer –$(A_xB_{1-x})_n$- is eventually described by combined descriptors of their monomers in eq (3), with the first elements of the descriptor vector stemming from the summing, and the last ones from the absolute differences of (molar ratio-weighed or not) monomer descriptors.

$$\overrightarrow{D^x} = \left[xD_{A,i} + (1-x)D_{Bi}, i = 1 \ldots N; |xD_{Ai} - (1-x)D_{Bi}|, i = 1 \ldots N\right] \tag{3}$$
$$\overrightarrow{D^0} = \left[D_{A,i} + D_{Bi}, i = 1 \ldots N; |D_{Ai} - D_{Bi}|, i = 1 \ldots N\right]$$

where D_A and D_B are the descriptor values of the individual monomers A and B, respectively, while x is the molar fraction of the first listed monomer, A and N the dimension of descriptor D in the chemical space containing all monomers, irrespective of their reactive class. Polymer descriptors will thus have a maximal dimensionality of 2N – and typically much less, noting that in the case of homopolymers the absolute difference contributions will systematically be zero. Since, for each of the 87 different fragmentation schemes applied to monomers, the two distinct combination strategies – with and without accounting of molar ratio – are applied, a total of 168 distinct descriptor spaces competed in the evolutionary strategy to be selected as the best support for optimally cross-validating Support Vector Machine models, *vide infra.*

4-2-4. Building and validation of the models

SVR models were built and validated using the ε-SVR algorithm implemented in the libSVM package.[42] Optimally parameterized SVR models, including descriptor choice as a key degree of freedom, were built according to the evolutionary procedure,[43] which provides both descriptor space selection and optimization of the operational parameters (epsilon, kernel type, cost, gamma) of the SVR method. The SVR models have been built for homopolymer, copolymer, and general data sets.

The predictive performance of the SVR models has been estimated by squared determination coefficient calculated in three-fold cross-validation (Q^2) repeated 12 times after the data reshuffling (12 × 3-CV) and eventually on the external test set (R^2) which are shown in eq 2, and Root-Mean-Squared Error (RMSE) which is shown in eq 3.

$$Q^2(R^2) = 1 - \frac{\sum_{i=1}^{n}(Y_{exp,i} - Y_{pred,i})^2}{\sum_{i=1}^{n}(Y_{exp,i} - \langle Y \rangle_{exp})^2} \tag{4}$$

$$RMSE = \sqrt{\frac{\sum_{i=1}^{n}(Y_{exp,i} - Y_{pred,i})^2}{n}} \tag{5}$$

Here Y_{exp} and Y_{pred} are experimental and predicted values of T_g respectively, n is the number of data points, while $\langle Y \rangle_{\mathrm{exp}}$ is the mean of experimental values.

4-2-5. Generative Topographic Mapping

Generative Topographic Mapping (GTM) is a nonlinear mapping method used for data visualization originally described by Bishop.[26] In GTM, a 2D latent space (called manifold) is embedded into the descriptor space. The manifold represents a grid of k × k nodes; each node is mapped in the initial descriptor space using the mapping function y(x, W). The mapping function is given as a grid of m × m radial basis functions (RBFs). To build a GTM-based QSAR model, the weighted average of properties of all molecules associated with any particular node is used to "color" the manifold according to that property, achieving a meaningful separation of items with different properties, or assignable to different classes. Here, the map parameters were tuned in order to achieve maximization of the separations of the different polymer classes as given in the literature[2,6] (Table 4-1, listing 17 distinct polymer types assigned to both training and test items). Map tuning followed the evolutionary procedure already described, using only the five descriptor spaces employed in SVM models as potential candidates for the GTM descriptor space and addressing the classical tunable GTM parameters (the number of RBF kernels, the number of grid points, the width factor of radial basis functions, and the regularization coefficient). The global model training set served both as frame set (items to guide the fitting of the manifold in descriptor space) and selection sets (providing items to be optimally separated on the map – here, by chemical class). The optimality criterion was the mean ability to separate (balanced accuracy; BA) members from non-members of the 10 most well-represented polymer classes (with at least 10 examples in the global model training set) following the cross-validated projection of the global training set on the current manifold. Once an optimal manifold in the above-mentioned sense was selected, it was also "colored" by T_g values, leading to a coherent landscape with "red" and "blue" zones populated by high and low T_g polymers, respectively. White zones represent unpopulated areas.

Table 4-1. 17 classes of polymer and numbers of polymers in train/test set for each class.

Classes		Numbers of data	
		Train	Test
1	Epoxy resin	50	17
2	Polyolefin	15	3
3	Polystyrene	13	36
4	Polyvinyl	24	10
5	Polyacrylic	30	13
6	Polyhalo-olefin	9	2
7	Polydiene	5	5
8	Polyether	17	6
9	Polysulphide	2	0
10	Polyester	12	11
11	Polyamide	4	15
12	Polyimide	20	0
13	Polyamide-imide	1	0
14	Polycarbonate	26	1
15	Polyimine	20	0
16	Silicon-containing polymer	14	0
17	Polyxylene	8	0

4-3. Results and Discussion

4-3-1. Reproducibility of Katritzky's results by the proposed modeling strategy

The results of the Katritzky set model are shown in Table 4-2. The descriptor set producing the SVR model of maximal robustness (estimated by 3-CV Q^2 value) was based on atom-centered fragments of the length 1–3 (See Table S1). This model returned a Q^2 value of 0.727, RMSE of 34.3 K, with the worst misprediction error of 110.4 K. In previous works by Katritzky et al., T_gs for homopolymers calculated from predicted T_g/M values reported a Q^2 value of 0.754 based on 3-CV model, and a worst error of 111 K. Our results are consistent with Katritzky's, which means that SVR modeling with purely topological ISIDA fragment counts for homopolymers works as well as the more sophisticated model employing constitutional, geometrical, and quantum chemical descriptors. Although T_g/M was the property modeled by Katritzky, we can directly predict the T_g values. Most important, note that in Katritzky's work a "homopolymer"-specific strategy was used, focusing on the repeating unit in the polymer – which means that copolymers may only be predicted if they are 1:1 linear concatenation products of the two monomers. A polyamide is modeled as a "homopolymer" of the amide unit -C(=O)-A-C(=O)N-B-N- in Katritzky's approach, while the same species is rendered as a genuine heteropolymer in this work. The proposed descriptor scheme is thus robust in supporting simultaneous processing of genuine homopolymers and 1:1 linear copolymers, without the need to explicitly generate the repeating unit.

Table 4-2. T_g predictive accuracy from 12 × 3-CV models for Katritzky's, epoxy resin, and global training sets.

	Katritzky's set model	Epoxy resin-specific model	General model
Number of data points	88	50	270
T_g range /K	190–409	280–531	130–685
Q^2	0.727	0.864	0.920
RMSE /K	34.3	21.5	34.3
Max error /K	110.4	44.0	137.2

4-3-2. Epoxy resin-specific model

The results of the epoxy resin specific model are shown in Table 4-2. The descriptor set producing the SVR model of maximal robustness (estimated by 3-CV Q^2 value) was based on atom-centered fragments of the length 1–4 with AtomPairs option (See Table S1). This model performed well with a Q^2 value of 0.864, RMSE of 21.5 K, with the worst misprediction error of 44.0 K. In the previous work by Morrill,[21] the leave-one-out cross-validated coefficient of determination was 0.995, which is higher than our Q^2 result. The difference between the number of data set and the diversity of epoxy resin can be parts of the reasons why our Q^2 value were lower than the Morrill's result. 50 epoxy resins are contained in our data set, on the other hand, Morrill's data set has only 13 data points. Additionally, there was small diversity of epoxy resin in Morrill's data base because Morrill et al. applied only DGEBA for their prediction as a representative epoxy resin, while we have 6 kinds of epoxy resin in training set. Comparing with Katritzky's set model (section 3.1), epoxy resin-specific model returned higher accuracy. There are two possibilities for the reason. (1) Because the number of data points decreased, regression model fitted on data points more exactly. Since if the model fits too exactly to a particular data set, the model fails to fit additional external test set, we have checked the reliability of our model by using scrambled T_g data set to avoid this risk. T_gs were randomly mixed to create no correlated epoxy resin–T_gs data set. The same procedure as epoxy-specific model of SVR modeling was applied to this data set, at least it is proved that epoxy-specific model was not overfitting model although the number of the data set was relatively small. (2) Basically epoxy–amine copolymers have similar structures; all of epoxies have epoxy group, most of them also contain benzene rings, and all of amines contain amine groups. Therefore, the prediction should be more accurate than Katritzky's data set which has big diversity and different chemical groups. The similarity of epoxy resin structures will be assured by GTM maps discussed in section 2.4.

A consensus model was generated from 5 models which showed high robustness to predict 17 epoxy resins of external test set. The 5 different models have several types of descriptor set; two of them contain the sequence of the length within 2–6 with FormalCharge and AtomPairs options, other two contain atom-centered fragments of the length within 1–3 with FormalCharge, and another model is based on the sequence of the length 2–7. Descriptors in former 4 models were not multiplied by molar ratio, while descriptors in the last model were multiplied by molar ratio (See Table S2). Prediction of the external test set have returned an R^2 value of 0.687, RMSE of 22.3 K, with the worst misprediction error 50.2 K. In the previous work by Bellenger et al.,[20] "The results, which are given in Table V, are generally in good agreement with the experimental data; the average error of the prediction being less than 3%." To compare with this, our results showed the average error of the prediction less than 4% which is relatively acceptable.

4-3-3. General model

To create the general model, 132 linear homo/heteropolymers set have been added to combined Katritzky's data set and epoxy resin set as training data. The results of the general model are shown in Table 4-2. This model performed with a Q^2 value of 0.920, RMSE of 34.3 K, with the worst misprediction error of 137.2 K. The plot of predicted T_g values versus experimental T_g values is shown in Figure 4-4. The descriptor set producing the SVR model of maximal robustness (estimated by 3-CV Q^2 value) was based on atom-centered fragments of the length 1–3 with FormalCharge option (See Table S1). This model returned higher accuracy than epoxy resin-specific model. The increasing number of data points must have affected Q^2 high accuracy, since Q^2 was improved even though the diversity of data points much wider than Katritzky's set model and epoxy resin-specific model.

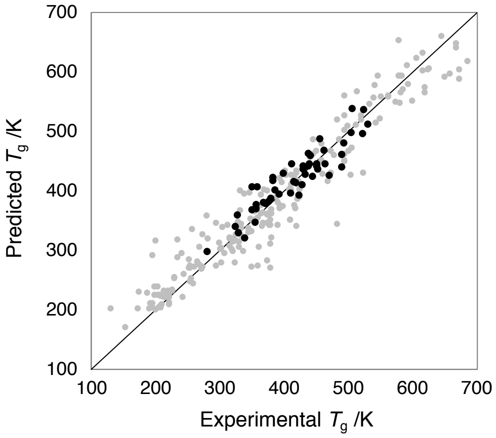

Figure 4-4. Plot of predicted T_g values versus experimental T_g values for 270 training data set consisted of 220 linear homo/heteropolymers (gray) and 50 epoxy resins (black) from 12 × 3-CV prediction.

The external test set consisted of 102 linear homo/heteropolymers from Bicerano's data set and 17 epoxy–amine copolymers from Bellenger's data set were predicted from a consensus model generated from 5 models which showed high robustness. The 5 models which is the base of the consensus model have atom-centered fragments of the length within 1–4, additionally one of them contained FormalCharge option (See Table S2). This external validation showed results of an R^2 value of 0.779, RMSE of 35.9 K, with the worst misprediction error of 127.1 K. The plot of predicted T_g values versus experimental T_g values is shown in Figure 4-5. We have divided the test set into linear polymer part and epoxy resin part to check each accuracy. The breakdown is shown in Table 4-3 together with external validation results of epoxy resin-specific model (section 3.2). As shown in Table 4-3, general model succeeded to improve the prediction accuracy of epoxy resin part of test set comparing with results of epoxy resin-specific model. It is interesting that the model could get better results for the epoxy resin prediction when homo/heteropolymers have been added into training set. According to both results of 3-CV for training data set and external validation for test set, the greater diversity of polymer structures can be considered to lead to the better T_g predictions. Generation of model based on such diverse database consisted of homo/heteropolymer and cross-linked epoxy resins has never been attempted before, and we found this general model for global set can predict T_gs with better accuracy especially for epoxy resins. Originally, epoxy resins exist relatively less than other polymers which makes difficult to get big data for machine learning, and our discovery would be also helpful from that point of view.

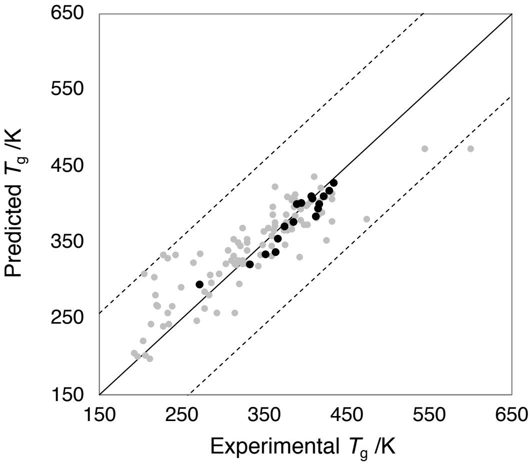

Figure 4-5. Plot of predicted T_g values versus experimental T_g values for 119 external data set consisted of 102 linear homo/hetero polymers (gray) and 17 epoxy resins (black).

Table 4-3. Results of external test set based predicted from consensus models of epoxy resin set and global set. For general model, results for the entire set and breakdown consisted of linear polymer and epoxy resin parts are shown.

	General model			Epoxy resin-specific model
	All	Linear polymer	Epoxy resin	
Number of data points	119	102	17	17
R^2	0.779	0.761	0.848	0.687
RMSE /K	35.9	38.3	15.6	22.3
Max error /K	127.1	127.1	29.6	50.2

4-3-4. Polymer space analysis by GTM visualization

16 GTMs highlighting the (fuzzy) separation of members from non-members of all classes except class 9 are shown in Figure 4-6. Class 9 has been removed since there are only two polysulfides in this data set, as shown in Table 4-1. The map supporting these fuzzy classification landscapes is based on atom-centered fragments of restricted atoms and bonds with a length of 1–3, with multiplication by molar ratio. All compounds (training set and test set of global set confounded) have been projected. Most classes are indeed well separated from each other (BAs for 10 most well-represented polymer classes in the cross-validated projection of the global training set were more than 0.88, such as 1.00 for class 1, 0.98 for class 5 and 12), which means that the selection of descriptors was well chosen by GA in SVR modeling. In particular, members of Class 1 and 5 are nearly perfectly separated from any other classes. This is not surprising for epoxy resins, which indeed stand out as the only (potentially) reticulated polymers for which T_g data were available.

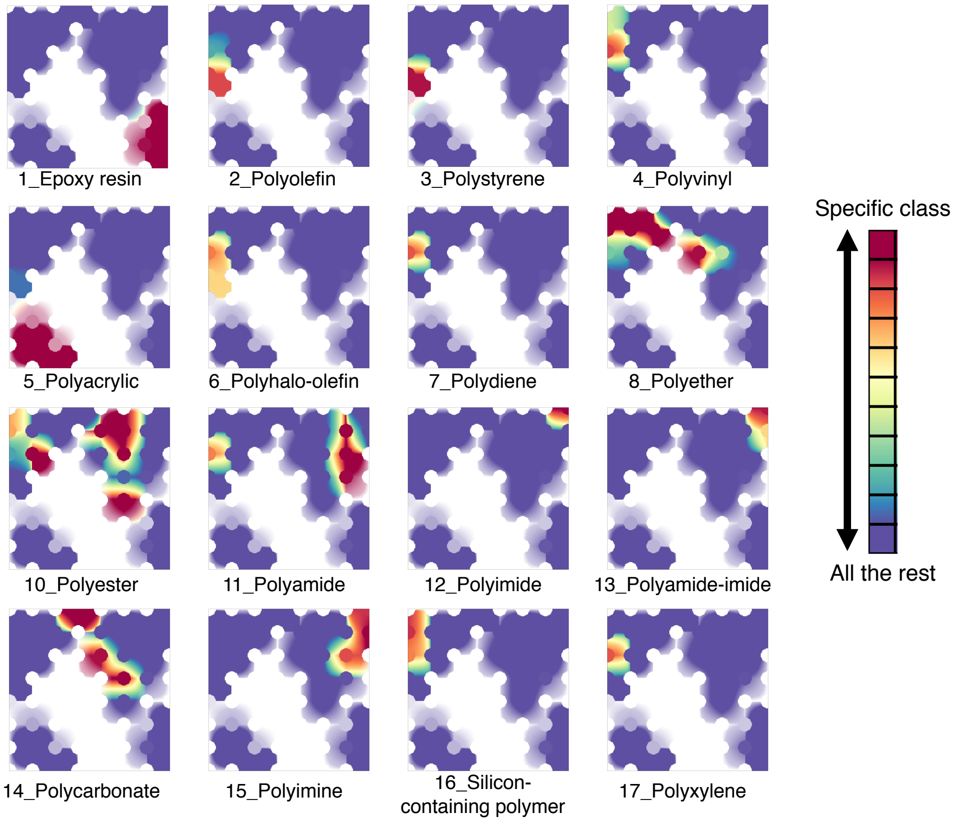

Figure 4-6. Polymer class landscapes for 16 classes for training and test set of global data set. Red area represents compounds in the specific class, while violet area represents all the rest compounds in other classes. Density of compounds on each node were expressed by the density of color.

Some polymer classes do however overlap to significant extents, but this can be perfectly well explained on behalf of the chemical similarity of structures, which transcends the rather rigid labelling by chemical class. Classes 2 to 7 are homochain polymers which are classified based on the type of side chains, while 8 to 17 are heterochain polymers which contains some elements or chemical groups in main chain such as oxygen, sulfur, carbonyl group amide group, benzene rings. They are classified based on the type of main chain. Overlap on the map may arise because of the similarity of either main chains or side chains. Unsurprisingly, "polycarbonates" and "polyesters" are overlapping – carbonates are technically esters of the carbonic acid, after all. Also, the distinction between "Polyvinyl" compounds and "Polyhalo-olefins" is not clear – neither is the separation of these two classes. More interesting is the case of overlapping classes 7 (polydiene) and 17 (polyxylene). Clearly, one would expect aromatic polyxylenes to be distinct from polydienes – however, the formal monomers (Figure 4-7) used to describe polyxylene formation are, too, nothing but polyenes. Aromaticity is an unpredicted consequence of the reaction – therefore, the reagent-based similarity of the two classes – the underlying reason of the observed overlap – is not reflected in the final product. This is a limitation on (formal) monomer-based representation advocated here in order to unify modeling of T_g for both linear and reticulated polymers. Regardless of this, the T_g landscape shown in Figure 4-8 indicate that compounds on node 3 and surrounding nodes have relatively low values compared to the global T_g range. (Strictly speaking, it should be noted that the T_g ranges are 171–293 K for class 7, 298–373 K for class 17, they are not overlapping.) On the opposite, significant diversity may occur within a chemical class. For example, compounds of class 10 spread on some nodes of the map because some of them have normal carbon chain, others have benzene rings with ester groups in the main chain (Figure 4-9).

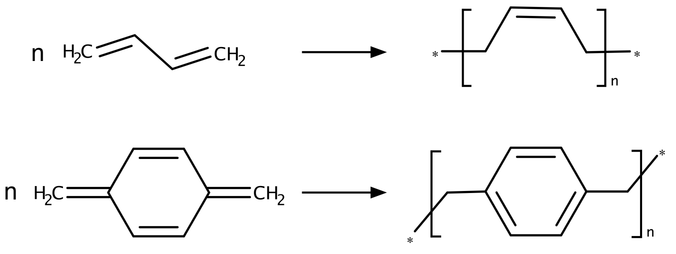

Figure 4-7. Polymerization of class 7 (polydiene) and class 17(polyxylene).

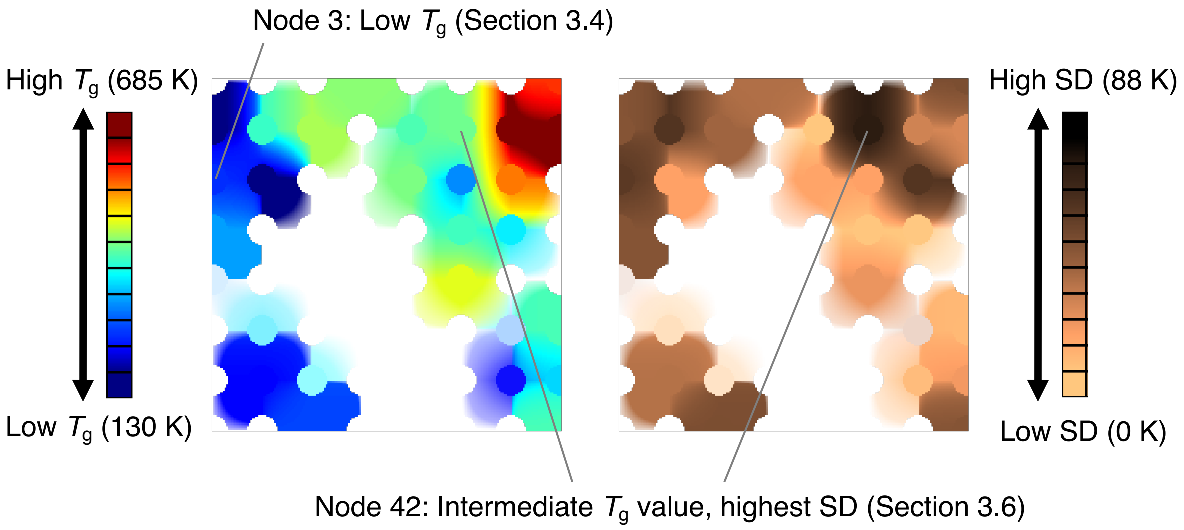

Figure 4-8. T_g landscape (left) and the landscape of the T_g standard deviation (SD) at each node (right).

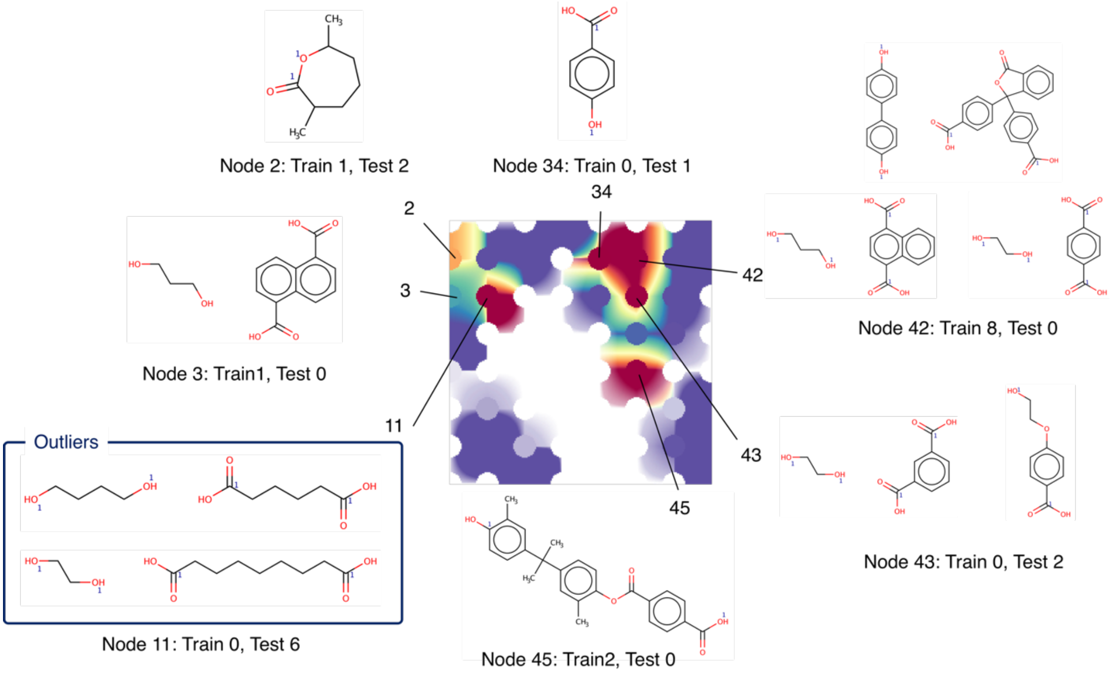

Figure 4-9. Representative structures, the number of training/test on each node of the map for class 10.

4-3-5. Understanding outliers within their chemical space context

According to the external validation of the SVR model in section 2.3, three outliers were evidenced: two polyesters (class 10) and one polyamide (class 11). Figure 4-9 and Figure 4-10 show landscapes of classes 10 and 11, representative structures, and the number of training/test set compounds residing in each node. Or, the nodes in which these outliers reside do not harbor any training set compounds. In other words, if the GTM model would have been used as Applicability Domain delimiter, these outliers would have counted as excluded from the AD. Note that they did pass the less stringent test of "fragment control" used by the SVR model, but they do not stand out in terms of rare fragments – they rather stand out in terms of how these fragments are interconnected. Aliphatic diacids and diols are well represented in the training set – yet, their combinations are not. Table 4-4 shows the accuracy of T_g predictions for test set compounds of class 10 and 11 based on SVR general model in section 2.3. Although the worst misprediction error of class 11 is higher than that of class 10, RMSE and R^2 values of class 11 were much better than for class 10, regardless of the fact that class 10 has relatively more training set data than class 11. As discussed above, the imbalance coverage of polymer chemical space by train/test data is the reason for this. According to Figure 4-9, most of test data of class 10 is on node 11, which does not have any training item residing here. On the other hand, in Figure 4-10, most of test data resides in node 3, which is the residence node of one training item with a T_g value matching rather closely the ones of external compounds. As a consequence, their T_g predictions were quite accurate.

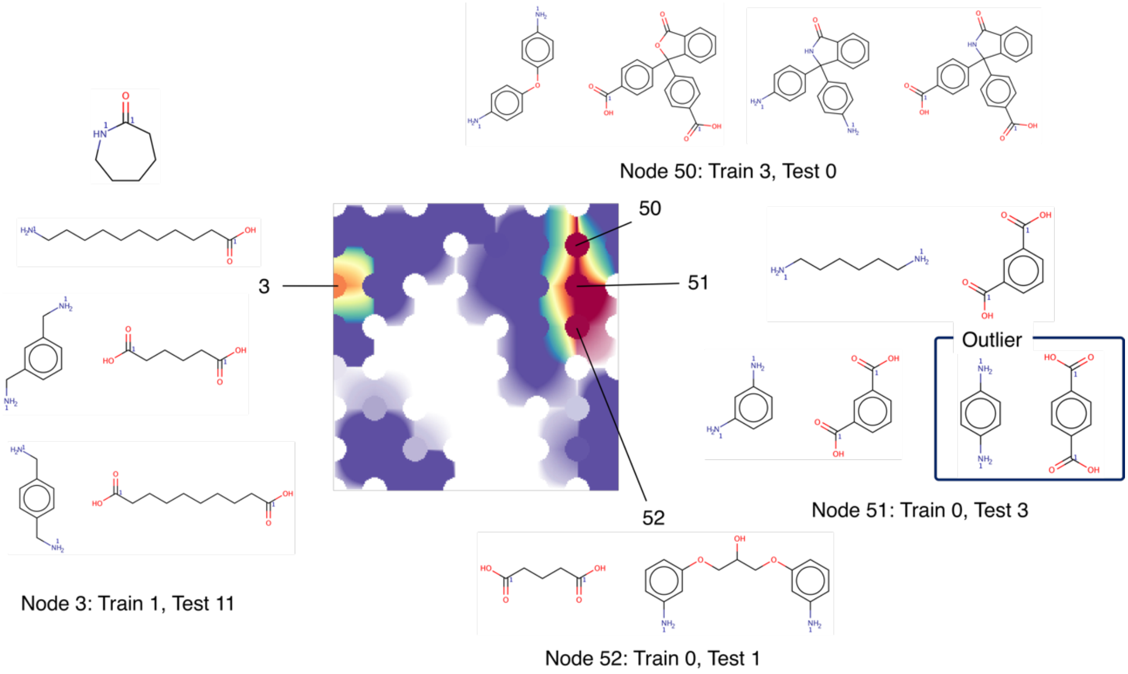

Figure 4-10. Representative structures, the number of training/test on each node of the map for class 11.

Table 4-4. External validation results from SVR general model in section 2.3. for each class 10 and 11.

Classes		Numbers of data		Accuracy of Tg prediction for test data on general model		
		Train	Test	R^2	RMSE	Max Error
10	Polyester	12	11	–0.18	72.6	105.7
11	Polyamide	4	15	0.73	44.5	127.1

4-3-6. The T_g Landscape of Polymer Space

A key advantage of GTM is that a convenient manifold may be used to support any arbitrary property landscape. Even though the map was chosen for its propensity to separate chemical classes of polymers, it is nevertheless able to display a T_g landscape, with clearly separated high- and low-temperature areas. It is important to note upfront that, since the color code reflects averages of T_g values projected on each node, the interpretation of both high and low temperature nodes is straightforward: these chemical space zones are predominantly populated by polymer with extremal (high, respectively low) T_g values. By contrast, zones with "medium" T_g corresponding to intermediate spectral colors might arise either due to a local concentration of polymers with intermediate T_g values, or due to the cohabitation of low- and high-temperature polymers. To lift this uncertainly, the T_g landscape can be associated to the landscape of the T_g standard deviation at each node (Figure 4-8). The node with the highest divergence of T_g values of residing polymers can be clearly located in the Figure. The eight residents therein have a mean T_g of 435.0 ± 88 K. In all other nodes, resident polymers have better focused T_g ranges.

In Figure 4-11, low T_g areas (in blue) in the North-West (top left) mainly accommodate simple carbon polymers. Moving North, mean T_g values correspond to compounds contain oxygen, carbonyl groups, or carboxyl group. Eventually, the North-East is a high T_g-area, populated with polyamides and -imines. It is thus apparent that structure similarity as captured by the map implies similarity of T_g values. While the polymer class is *per* se a partial indicator of expectable T_g values, the map (and, of course, the predictive models) provide additional accuracy. In particular, epoxy resins form a well-separated class of polymers with strongly varying T_g values. This variability is well reproduced by the map, which provides a fine split of class 1 epoxy resins into subfamilies of higher and lower T_g, depending on their degree of reticulation. On the other hand, in the case of class 5, there can be special reason why they were well separated even though they have similar T_g ranges from top left compounds on the map, which can be interesting topic to investigate in detail for the future work.

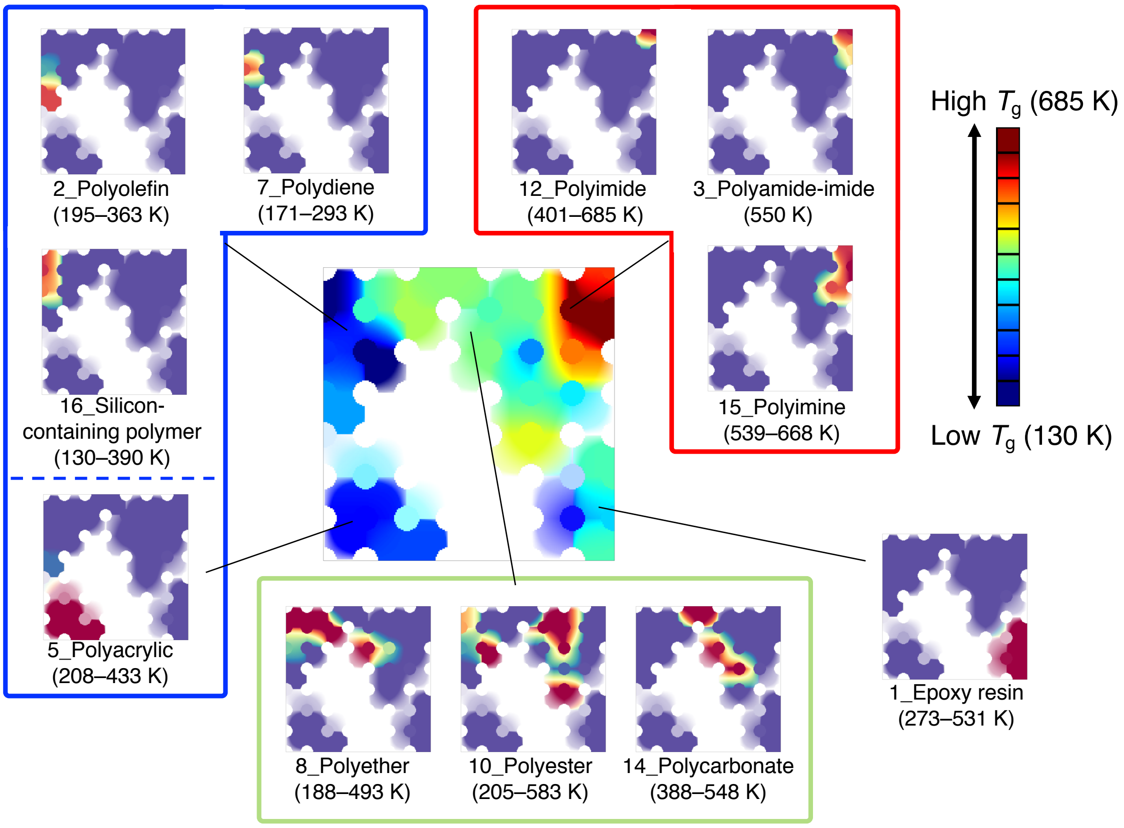

Figure 4-11. T_g landscape and representative maps on some areas depending on the T_g values.

4-4. Conclusions

The successfully addressed challenge of this work was to propose a unified framework for chemoinformatics modeling of the glass transition temperature T_g of both reticulated and linear homo- and heteropolymers, which were traditionally addressed by distinct approaches. The key to solve this problem was the unified description paradigm of these polymers, by means of molar-ratio-sensitive "mixing" of atom-marked ISIDA fragment counts of the "formal" monomers – following typical mixture modeling strategies, where in homopolymers the single monomer is considered in 1:1 "mixture" with itself. This "formal monomer"-based strategy accommodates both linear and reticulated polymers, while classical approaches based on descriptors of the repeating unit only work for linear homo- and 1:1 heteropolymers $–(AB)_n–$, i.e. "homopolymers" of repeating unit AB. "Formal" monomers are rendered according to herein defined, specific standardization rules – following not the actual chemical mechanism of polymerization, but aiming to minimize the number of simplest schemes that could be used to formally describe the polymerization process. For example, aldehyde polymerization is easiest rendered as the formal polymerization of vinyl alcohol, the unstable tautomer of the aldehyde. This may be mechanistically untrue but has the merit to describe these polymers in a similar way to “other” polyolefins. This unified rendering of all polymers as pairs of monomers (identical, for homo- or different, for heteropolymers) was shown to apply even to some ternary polymers, if a judicious choice of formal monomers is made. The rule here is to minimize the number of marked atoms, involved in bonds being formed or changing bond order. While this rule is clearly established, it must be nevertheless pointed out that the herein performed standardization is semi-automatic and required human reflection and decision-making for specific cases. A fully automated implementation of rendering polymers by their “formal” monomers would require an additional technical development, which is not a priority knowing that, unlike drug-like molecules having structures that can be directly accessed from electronic databases, a universal standard for polymer databases is not yet established, making chemical name to structure conversion an unavoidably human intervention requiring step, anyway.

Starting from the file of pairs of monomers and molar ratio information, descriptor calculation, model building and prediction are fully automated, following standard QSAR procedures. In a first step, a focused approach excluding reticulated epoxy resins was challenged to reproduce Katritzky’s previous study and achieved comparable results. Specific modeling of epoxy resins (reticulated or not) also proved to be robust. Eventually, the general model covering both linear homo/heteropolymers and cross-linked epoxy resins showed the highest accuracy ($Q^2 = 0.920$, RMSE = 34.3 K for training set of 270 polymers, and $R^2 = 0.779$, RMSE 35.9 K for external test set of 119 polymers) of three models. Especially, this model performed better predicting epoxy resins T_g than the dedicated, epoxy resin-specific model. The greater diversity of polymer structures has thus a significant impact in improving T_g predictions *across* polymer classes. Generation of models based on such a diverse database has never been attempted before, and it was shown to be helpful for improving predictions for small polymer families, where paucity of training data automatically limits the applicability domain of local, dedicated models.

Eventually, polymer space analysis using GTM landscapes highlighted several interesting insights. Outliers mispredicted during the external validation of the model, were shown to reside in chemical space zones with insufficient training data. GTM landscapes allow a clear separation of chemically distinct polymer families, but also highlighted an interesting case (polydienes *versus* polyxylenes) where monomer-based rendering was pushed to its limits – aromatization occurring during the polymerization process cannot be captured by monomer-based descriptors. The GTM may also harbor the landscape of the property of interest T_g herewith permitting the intuitive oversight of the association of polymer classes to glass temperature ranges.

Reference

1. Sperling, L. H. *Introduction to Physical Polymer Science*, 4th ed; John Wiley & Sons, Inc. New Jersey, 2006.
2. Bicerano, J. *Prediction of Polymer Properties*, 3nd ed.; Marcel Dekker, Inc. New York, 2002.
3. Mattioni, B. E.; Jurs, P. C. Prediction of Glass Transition Temperatures from Monomer and Repeat Unit Structure Using Computational Neural Networks. *J. Chem. Inf. Comput. Sci.* **2002**, *42* (2), 232–240.
4. Cheremisinoff, N. P. *Polymer characterization: laboratory techniques and analysis*; Noyes Publications, New Jersey, 1996.
5. Krause, S.; Gormley, J. J.; Roman, N.; Shetter, J. A.; Watanabe, W. H. Glass Temperatures of Some Acrylic Polymers. *J. Polym. Sci. Part A* **1965**, *3* (10), 3573–3586.
6. Van Krevelen, D. W. *Properties of polymers*, 4th completely revised ed.; Elsevier, Oxford, 2009.
7. Weyland, H. G.; Hoftyzer, P. J.; Van Krevelen, D. W. Prediction of the Glass Transition Temperature of Polymers. *Polymer* **1970**, *11* (2), 79–87.
8. Barton, J. M. Relation of Glass Transition Temperature to Molecular Structure of Addition Copolymers. *J. Polym. Sci. Part C* **1970**, *30* (1), 573–597.
9. Lee, W. A.; Establishment, R. A. Calculation of the Glass Transition Temperatures of Polymers. Part I. Homopolymers and Copolymers with Alkyl Side Chains. *Polymer* **1970**, *8*, 555–570.
10. Wiff, D. R.; Altieri, M. S.; Goldfarb, I. J. Predicting Glass Transition Temperatures of Linear Polymers, Random Copolymers, and Cured Reactive Oligomers from Chemical Structure. *J. Polym. Sci., Part B, Polym. Phys.* **1985**, *23*, 1165–1176.
11. Hopfinger, A. J.; Koehler, M. G.; Pearlstein, R. A.; Tripathy, S. K. Molecular Modeling of Polymers. IV. Estimation of Glass Transition Temperatures. *J. Polym. Sci. Part B Polym. Phys.* **1988**, *26* (10), 2007–2028.
12. Koehler, M. G.; Hopfinger, A. J. Molecular Modelling of Polymers: 5. Inclusion of Intermolecular Energetics in Estimating Glass and Crystal-Melt Transition Temperatures. *Polymer* **1989**, *30* (1), 116–126.
13. Cypcar, C. C.; Camelio, P.; Lazzeri, V.; Mathias, L. J.; Waegell, B. Prediction of the Glass Transition Temperature of Multicyclic and Bulky Substituted Acrylate and Methacrylate

Polymers Using the Energy, Volume, Mass (EVM) QSPR Model. *Macromolecules* **1996**, *29* (27), 8954–8959.

14. Camelio, P.; Cypcar, C. C.; Lazzeri, V.; Waegell, B. A Novel Approach toward the Prediction of the Glass Transition Temperature: Application of the EVM Model, a Designer QSPR Equation for the Prediction of Acrylate and Methacrylate Polymers. *J. Polym. Sci. Part A Polym. Chem.* **1997**, *35* (13), 2579–2590.
15. Katritzky, A. R.; Rachwal, P.; Law, K. W.; Karelson, M.; Lobanov, V. S. Prediction of Polymer Glass Transition Temperatures Using a General Quantitative Structure-Property Relationship Treatment. *J. Chem. Inf. Comput. Sci.* **1996**, *36* (4), 879–884.
16. Katritzky, A. R.; Sild, S.; Lobanov, V.; Karelson, M. Quantitative Structure - Property Relationship (QSPR) Correlation of Glass Transition Temperatures of High Molecular Weight Polymers. *J. Chem. Inf. Comput. Sci.* **1998**, *38* (2), 300–304.
17. Cao, C.; Lin, Y. Correlation between the Glass Transition Temperatures and Repeating Unit Structure for High Molecular Weight Polymers. *J. Chem. Inf. Comput. Sci.* **2003**, *43* (2), 643–650.
18. Liu, W.; Cao, C. Artificial Neural Network Prediction of Glass Transition Temperature of Polymers. *Colloid Polym. Sci.* **2009**, *287* (7), 811–818.
19. Lee, G.; Hartmann, B. Glass Transition Temperature Predictions in Some Epoxy Polymers. *J. Appl. Polym. Sci.* **1983**, *28* (2), 823–830.
20. Bellenger, V.; Verdu, J.; Morel, E. Effect of Structure on Glass Transition Temperature of Amine Crosslinked Epoxies. *J. Polym. Sci. Part B Polym. Phys.* **1987**, *25* (6), 1219–1234.
21. Morrill, J. A.; Jensen, R. E.; Madison, P. H.; Chabalowski, C. F. Prediction of the Formulation Dependence of the Glass Transition Temperatures of Amine-Epoxy Copolymers Using a QSPR Based on the AM1 Method. *J. Chem. Inf. Comput. Sci.* **2004**, *44* (3), 912–920.
22. Varnek, A.; Fourches, D.; Horvath, D.; Klimchuk, O.; Gaudin, C.; Vayer, P.; Solov'ev, V.; Hoonakker, F.; Tetko, I.; Marcou, G. ISIDA - Platform for Virtual Screening Based on Fragment and Pharmacophoric Descriptors. *Curr. Comput. Aided-Drug Des.* **2008**, *4* (3), 191–198.
23. Ruggiu, F.; Marcou, G.; Varnek, A.; Horvath, D. ISIDA Property-Labelled Fragment Descriptors. *Mol. Inform.* **2010**, *29* (12), 855–868.

24. Ruggiu, F.; Solov'ev V.; Marcou, G.; Horvath, D.; Graton, J.; Le Questel, J. Y.; Varnek, A. Individual Hydrogen-Bond Strength QSPR Modelling with ISIDA Local Descriptors: a Step Towards Polyfunctional Molecules. *Mol.Inform.* **2014**, *33* (6–7), 477–487.
25. Drucker, H.; Burges, C. J.; Kaufman, L.; Smola, A.; Vapnik, V. Support Vector Regression Machines. *Advances in neural information processing systems* **1997**, *9*, 155–161.
26. Bishop, C. M.; Svenseń, M.; Williams, C. K. I. GTM: The Generative Topographic Mapping. *Neural Comput.* **1998**, *10*, 215– 234.
27. Kireeva, N.; Baskin, I. I.; Gaspar, H. A.; Horvath, D.; Marcou, G.; Varnek, A. Generative Topographic Mapping (GTM): Universal Tool for Data Visualization, Structure-Activity Modeling and Dataset Comparison. *Mol. Inf.* **2012**, *31*, 301−312.
28. Gaspar, H. A.; Baskin, I. I.; Marcou, G.; Horvath, D.; Varnek, A. GTM-Based QSAR Models and Their Applicability Domains. *Mol. Inf.* **2015**, *34*, 348−356.
29. Cook, W. D.; Mayr, A. E.; Edward, G. H. Yielding behaviour in model epoxy thermosets – II. Temperature dependence. *Polymer* **1998**, *39* (16), 3725–3733.
30. Chen, M. C.; Hourston, D. J.; Sun, W. B. Miscibility and Fracture Behaviour of an Epoxy Resin-Bisphenol-A Polycarbonate Blend. *Eur. Polym. J.* **1992**, *28* (12), 1471−1475.
31. Lee, J. Y.; Shimb, M. J.; Kim, S. W.; Characteristics of the DGEBA/MDA system modified with glutaronitrile. *Mater. Chem. Phys.* **1996**, *44*, 74–78.
32. Knorr, D. B.; Yu, J. H.; Richardson, A. D.; Hindenlang, M. D.; McAninch, I. M.; La Scala, J. J.; Lenhart, J. L. Glass Transition Dependence of Ultrahigh Strain Rate Response in Amine Cured Epoxy Resins. *Polymer.* **2012**, *53*, 5917–5923.
33. Bellenger, V.; Dhaoui, W.; Morel, E.; Verdu, J. Packing Density of the Amine-Crosslinked Stoichiometric Epoxy Networks. *J. Appl. Polym. Sci.* **1988**, *35*, 563–571.
34. Carfagna, C.; Apicella, A.; Nicolais, L. The Effect of the Prepolymer Composition of Amino-Hardened Epoxy Resins on the Water Sorption Behavior and Plasticization. *J. Appl. Polym. Sci.* **1982**, *27*, 105–112.
35. Chang, T. D.; Carr, S. H.; Brittain, J. O. Studies of Epoxy Resin Systems: Part A: A Study of the Origins of the Secondary Relaxations of Epoxy Resins by Thermally Stimulated Depolarization. *Polym. Eng. Sci.* **1982**, *22* (18), 1205–1212.
36. Garcia, F. G.; Soares, B. G.; Pita, V. J. R. R.; Sánchez, R.; Rieumont, J. Mechanical Properties of Epoxy Networks Based on DGEBA and Aliphatic Amines. *J. Appl. Polym. Sci.* **2007**, *106*, 2047–2055.

37. Perret, B.; Schartel, B.; Stöß, K.; Ciesielski, M.; Diederichs, J.; Döring, M.; Krämer, J.; Altstädt, V. A New Halogen-Free Flame Retardant Based on 9,10-Dihydro-9-oxa-10-phosphaphenanthrene-10-oxide for Epoxy Resins and their Carbon Fiber Composites for the Automotive and Aviation Industries. *Macromol. Mater. Eng.* **2011**, *296*, 14–30.
38. Gumen, V. R.; Jones, F. R.; Attwood, D. Prediction of the Glass Transition Temperatures for Epoxy Resins and Blends Using Group Interaction Modelling. *Polymer.* **2001**, *42*, 5717–5725.
39. Zhou, J.; Lucas, J. P. Hygrothermal Effects of Epoxy Resin. Part II: Variations of Glass Transition Temperature. *Polymer.* **1999**, *40*, 5513–5522.
40. Pineda, Á. F. E.; Garcia, F. G.; Soares, B. G.; Simões, A. Z.; Silva, E. L. Comparative Study of Glycerol Diglycidyl Ether/Aliphatic Amines Networks. *EIJST.* **2017**, *6* (7), 48–65.
41. Available from: http://infochim.u-strasbg.fr/
42. Chang, C.; Lin, C.; Tieleman, T. LIBSVM : A Library for Support Vector Machines. *ACM Trans. Intell. Syst. Technol.* **2008**, *307*, 1–39.
43. Horvath, D.; Brown, J.; Marcou, G.; Varnek, A. An Evolutionary Optimizer of Libsvm Models. *Challenges* **2014**, *5* (2), 450–472.

Chapter 5. General Conclusions

In this thesis, we focused on epoxy resins and analyzed the polymer matrix computationally. In chapter 2 and 3, *ab initio* calculations were utilized to investigate adhesive properties at the epoxy resin/silica interface. In chapter 4, on the other hand, chemoinformatics was used for the T_g prediction of 389 types of polymers including 67 types of epoxy resins.

In chapter 2, we theoretically investigated the adhesion interface between glass fiber and epoxy resin by constructing interfacial models under normal conditions. To clarify intermolecular interactions working at the adhesion interface, periodic DFT calculations were applied to slab models consisting of a fragment of epoxy resin and hydrophilic silica surfaces with or without adsorbed water molecules. Effects of water on the interfacial adhesion were evaluated on the basis of geometry-optimized structures, adhesion energies, and adhesion forces. We demonstrated that the adhesion properties are controlled by structural flexibility of the network of hydrogen bonds formed in the interface region as well as structural deformation of the hydrogen-bonding network of water molecules confined in the tight space between adhesive and adherend.

In chapter 3, we have extended our previous epoxy resin/silica model to a layer model (Layer-cluster model) for further investigation of interfacial interaction between epoxy resin and silica surface. PIEDA calculations led us to the conclusion that synergistic effects of the electrostatic and dispersion interactions are important in the Layer-cluster model. It was also found that the epoxy resin layer in the region of about 3.6 Å from the silica surface accounted for more than 99% of the total interfacial interaction.

In chapter 4, we have explored a unified approach to predict T_gs of linear homo/hetero-polymers and cross-linked epoxy resins by machine-learning approaches based on descriptors of reagents undergoing polymerization, represented in a formal way such as to encompass all the three scenarios: linear homo- and heteropolymers, plus reticulated heteropolymers.

Our research indicates the great potential of computational studies in the field of polymer chemistry. Studies in this thesis are still not enough to reach the critical answer that experimentalists require. There are still many factors that should be added into our investigation, such as curing agent in the epoxy resin. The polymer lateral distortion is also important to reproduce the shear test, which is the general measurement of adhesion strength in the experimental field. Our studies are only just the beginning. All we need to pay attention from now on is finding precise phenomenon that experimentalists eager to know and setting up more realistic models that can provide proper answer for them. Studies in this thesis will help those new studies as applicable skills and references to check basic theories. The author expects further development of computational chemistry on adhesion in the near future and fusion of theoretical and experimental research.

Publication List

1) Yoshizawa, K.; Semoto, T.; Hitaoka, S.; Higuchi, C.; Shiota, Y.; Tanaka, H. Synergy of Electrostatic and van Der Waals Interactions in the Adhesion of Epoxy Resin with Carbon-Fiber and Glass Surfaces. *Bull. Chem. Soc. Jpn.* **2017**, *90*, 500–505.

2) Higuchi, C.; Tanaka, H.; Yoshizawa, K. Molecular Understanding of the Adhesive Interactions between Silica Surface and Epoxy Resin: Effects of Interfacial Water. *J. Comput. Chem.* **2019**, *40*, 164–171.

3) Higuchi, C.; Horvath, D.; Marcou, G.; Yoshizawa, K.; Varnek, A. Prediction of the Glass-Transition Temperatures of Linear Homo/Heteropolymers and Cross-Linked Epoxy Resins. *ACS Appl. Polym. Mater.* **2019**, *1*, 1430–1442.

4) Higuchi, C.; Yoshizawa, K. Pair Interaction Energy Decomposition Analysis (PIEDA) of the Epoxy Resin/Silica Adhesive Interface, to be submitted.

5) 樋口千紗, 吉澤一成,「炭素とエポキシ樹脂の接着に関する量子力学的接着理論」機能材料, **2016**, *36*, 9–16.

6) 樋口千紗, 吉澤一成,「ガラス表面とエポキシ樹脂の接着に関する分子論的研究」NEW GLASS, **2020**, *35*, 16–18.

List of presentation at international conferences:

1) Chisa Higuchi, Hiromasa Tanaka, and Kazunari Yoshizawa, *2018 IMCE International Symposium*, Fukuoka, Japan, (March 16, 2018), Poster Presentation.

2) Chisa Higuchi, Hiromasa Tanaka, and Kazunari Yoshizawa, *16th International Congress of Quantum Chemistry*, Menton, France, (June 19, 2018), Poster Presentation.

Acknowledgements

The writing of this dissertation would not have been possible without the help and encouragement of many teachers, colleagues, and friends. It is my great pleasure to thank these people.

The author would like to express her cordial gratitude to Professor Kazunari Yoshizawa, for leading me to fascinating research field, adhesion. She is happy to express her appreciation to Associate Professor Yoshihito Shiota and Assistant Professor Yuta Tsuji for their helpful advice and suggestions. Special acknowledgments should be made to Associate Professor Hiromasa Tanaka at Daido University, for his kind advice, discussions, and helpful support.

It is a great pleasure to express her gratitude to Professor Alexandre Varnek at Strasbourg University, for welcoming her to his lab for the overseas training and supporting her during my stay in Strasbourg, France. She would like to thank Assistant Professor Gilles Marcou for his helpful discussion of Chemoinformatics. She is deeply grateful to Senior Researcher Dragos Horvath for his help and advice for the study of T_g prediction of polymers with Chemoinformatics approach.

The author would like to acknowledge Program for Leading Graduate Schools Advanced Graduate Course on Molecular Systems for Devices for great support and giving me the chance to have various experiences including the overseas training. She is thankful to Dr. Fanny Bonachera for her great help and encouragement across the world. I thank Dr. Olga Klimchuk for her support. I express my appreciation to all other members of the Yoshizawa laboratory and the Varnek laboratory for their direct and indirect support. I thank all my friends for their encouragement and understanding. In the end, I would like to thank all my family for all their help and encouragement.

Fukuoka, December 2020

Chisa Higuchi